Chip-Based Brillouin Processing for Microwave Photonic Phased Array Antennas

Matthew Garrett, *Student Member, IEEE*, Moritz Merklein, and Benjamin J. Eggleton, *Fellow, IEEE*

***Abstract*—In this review paper, we provide perspectives on the implementation of high-performance, wideband, chip-based Brillouin microwave photonic processing subsystems for use in phased array antennas that require processing at every antenna element. We review recent advances in chip-scale Brillouin microwave photonic signal processing systems, including reconfigurable filters, frequency converters, tunable phase shifters, true time delays and microwave sources, which are key functionalities for phased array antennas. We discuss a roadmap for developments of Brillouin-based microwave photonic processors to reach the required performance and compact footprint for implementation in future dynamically reconfigurable phased array antenna systems.**

***Index Terms*—Stimulated brillouin scattering, microwave photonics, integrated photonics, phased arrays.**

I. Introduction

WIDEBAND and high frequency microwave systems are attracting significant interest for use with phased array antennas (PAAs) [1], [2], [3]. When these systems are combined with the ability to generate electronically steerable radiation patterns, unique functionalities, including high resolution radars [4], [5] capable of tracking multiple targets [6], and directed high data rate communications to multiple users [7] are enabled. Typically, the emitted radiation pattern of a PAA is controlled by changing the relative phase (or delay) between the radiating elements in a process that is referred to as beamforming [3], [8], [9]. To reduce the presence of side-lobes in the PAA radiation pattern, each antenna element is typically separated by half the operating wavelength [10], [11]. Consequently, the components used for beamforming and analog signal conditioning, which form the interface between subsequent frequency conversion and digitisation stages, must fit in the space between radiating elements; this becomes challenging at higher frequencies, for example above 15 GHz the element spacing is less than a centimeter.

Manuscript received 16 May 2022; revised 3 August 2022; accepted 5 August 2022. Date of publication 10 August 2022; date of current version 21 October 2022. This work was supported by Australian Research Council (ARC) Discovery under Grants DP190100992, DP200101893 and DP220101431. *(Corresponding author: Benjamin J. Eggleton.)*

The authors are with the The University of Sydney Nano Institute (Sydney Nano), Institute of Photonics and Optical Science (IPOS), School of Physics, The University of Sydney, Sydney, NSW 2006, Australia (e-mail: matt.garrett@sydney.edu.au; moritz.merklein@sydney.edu.au; benjamin.eggleton@sydney.edu.au).

Color versions of one or more figures in this article are available at https://doi.org/10.1109/JSTQE.2022.3197766.

Digital Object Identifier 10.1109/JSTQE.2022.3197766

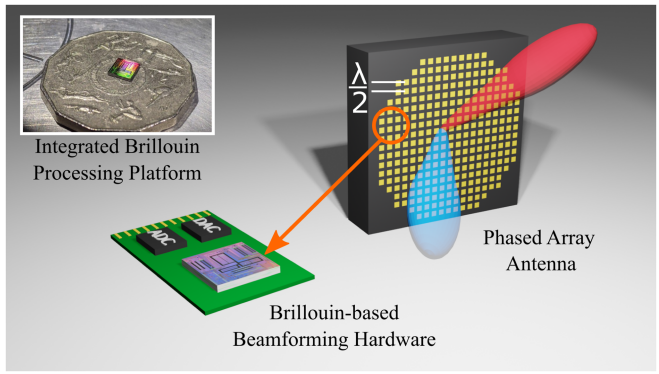

Fig. 1. Artistic impression of a phased array antenna which consists of radiating elements spaced by half the operating wavelength. On-chip Brillouin microwave photonic processing hardware is at each element to implement the required beamforming functionality. The inset shows a silicon photonic integrated circuit, a candidate hybrid platform for integrated Brillouin processing.

As an example, RF filters, a key component within PAAs, face challenges achieving wideband operation in the required compact form factor. Conventional RF filtering approaches based on surface and bulk acoustic wave processing achieve low losses and large out-of-band rejection [12]. However, they are not suitable for millimeter wave frequencies due to large acoustic losses [12], [13]. Reconfigurable filters based on cascaded banks of high-pass and low-pass filters offer discretely reconfigurable bandwidths and central frequencies [14]. However, many parallel filters are required to enable operation over a wide frequency range, increasing both system complexity and size. Filters based on ferromagnetic and ferrimagnetic materials, including yttrium iron garnet (YIG), achieve wide frequency tunability using compact cavities [15], [16], but require an external magnetic field to control their resonant frequency, complicating integration. While the above-mentioned devices exhibit impressive performance, there is no clear RF filter technology that can operate over a wide frequency range and be implemented in a compact footprint that is compatible with element-level processing for high frequency PAAs [1].

Microwave photonics (MWP) is well positioned to overcome the challenges associated with the increasing bandwidth and carrier frequencies [17] of next-generation wireless communications [18] and radar [19], [20] systems. Systems that utilise MWP signal processing achieve wideband and high frequency operation by transducing the RF signal into the optical domain using an electro-optic (E-O) modulator. The RF signal is then

processed using well established photonic components, that support operation over wide frequency ranges, before conversion back to the RF domain through photodetection [21]. The bandwidth of the MWP link is limited only by the bandwidth of the E-O modulator and photodetector (PD), which convert between RF and optical domains.

At the same time, photonic integrated circuits (PICs), based on established semiconductor fabrication techniques, are enabling significant reductions to the footprint of MWP devices [22], [23], [24], [25], [26], [27], opening possibilities for processing high frequency and wide bandwidth RF signals at every element of a PAA. Chip-based MWP devices have enabled demonstrations of numerous RF processing functionalities that could form the basis of future element-level processing required for PAAs, including agile RF filters [28], [29], phase shifters [30], [31] and true time delays (TTDs) for beam steering functionality, [32], [33], [34], frequency converters that interface between the operating RF and baseband frequencies [35], [36], and microwave sources [37], [38], [39], [40]. Initial demonstrations of MWP beamforming networks highlight the potential for implementing chip-based beamforming for PAAs [32], [34], [41], [42], [43], [44], expanded on below.

On-chip MWP processors, for example RF photonic filters, have been demonstrated using integrated optical micro-ring resonators (MRRs) [32], [45], [46]. Although good performance has been achieved, MRR-based processing has limited spectral flexibility, as the shape of the photonic resonance is determined by the intrinsic waveguide losses and fixed structural properties of the MRR. Alternatively, programmable photonic mesh processors offer flexible RF responses [47], [48], but increasing the number of mesh processors to support additional RF processing functionalities requires longer waveguide lengths, which comes at the expense of increasing RF losses and size [47]. MWP transversal filters can be created using multiple optical carriers propagating through on-chip dispersive delay lines [28], [49], but require many optical carriers to achieve sub-100 MHz processing [50], consequently increasing system complexity.

Integrated MWP beamforming elements highlight the advantages of photonic integration by enabling devices with compact form factors that operate at high frequencies and support wide RF signal bandwidths [32]. Chip-based MWP beamformers have been demonstrated using switchable delay lines [33], [51], but can only produce discrete delays, limiting beam steering flexibility. Continuously tunable delay lines have been implemented using broadband dispersive effects from waveguide gratings [52], [53], by changing the coupling ratios of MRRs [32], [34], [42], or using delay line interferometers [43]. However, these approaches lack the required frequency flexibility, agility and resolution due to the fixed device structural properties and difficulties in scaling the device size, as outlined above.

Stimulated Brillouin scattering (SBS) [54] has enabled microwave photonic signal processors with unmatched frequency selectivity, tunability, and reconfigurability [17]. Inducing SBS in chip-scale platforms greatly reduces the form factor of Brillouin devices, when compared to their fibre-based predecessors [55], [56], [57], [58]. SBS facilitates desirable fine spectral resolution (MHz-level), owing to the intrinsic narrow bandwidth of the Brillouin resonance, which exhibits a Lorentzian gain and loss response with narrow bandwidth of approximately 30 MHz [54], unmatched by other optical processing methods. Because the Brillouin resonance is optically induced, its spectral response can be dynamically reconfigured by tailoring the optical pump spectrum [59], [60], [61], enabling tailored filter shapes that can be tuned over multiple octaves. The narrow bandwidth resonant response of SBS forms the basis of programmable phase and amplitude control used in MWP processors and has been demonstrated in different chip-based platforms, including chalcogenide waveguides [62], [63], suspended silicon on insulator (SOI) waveguides [64], [65], [66], and high quality factor (Q) Si_3N_4 [67] and SiO_2 resonators [68].

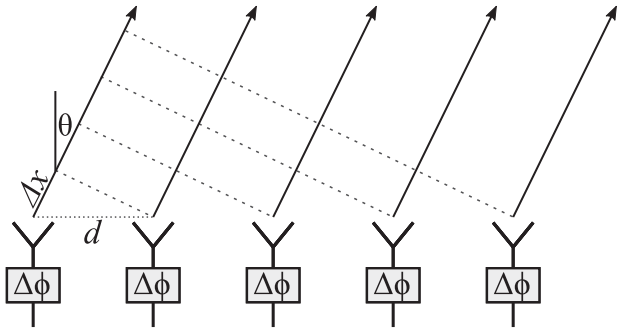

Fig. 2. Phased array antenna where beamforming is enabled by applying a phase shift to consecutive antenna elements.

In this paper, we review the recent advances in MWP processing systems that utilise on-chip SBS. We highlight key functionalities required for optical beamforming networks, including filters [29], [69], RF sources [70], [71], frequency converters [72], [73], phase shifters [74], [75], [76], and TTDs [77], [78]. We outline the challenges that must be overcome to enable a fully-integrated Brillouin-based beamforming network suitable for element-level processing in PAAs, and provide perspectives on technical improvements that must be made to achieve the long-term performance goals for MWP processors [29], [79].

II. Phased Array Antennas

PAAs are widely used in communications [7] and radar [5], [80] systems, enabling the transmission and reception of RF energy in an electronically controllable manner. Traditionally, PAAs consist of a two-dimensional array of antenna elements spaced by half the operating wavelength, as shown in the artistic impression in Fig. 1, which depicts a chip-scale Brillouin processor that implements beamforming at each PAA element. The inset shows a compact silicon-based hybrid photonic circuit, which is a candidate technology for the Brillouin processor that we outline in Section V.

Beamforming can be implemented in PAAs by introducing a phase shift, $\Delta\phi$, between elements as shown in Fig. 2. To direct the beam to an angle of θ, each successive wavefront must be delayed an additional path Δx, given by [5], [9], [80],

$$\Delta x = d \sin(\theta), \tag{1}$$

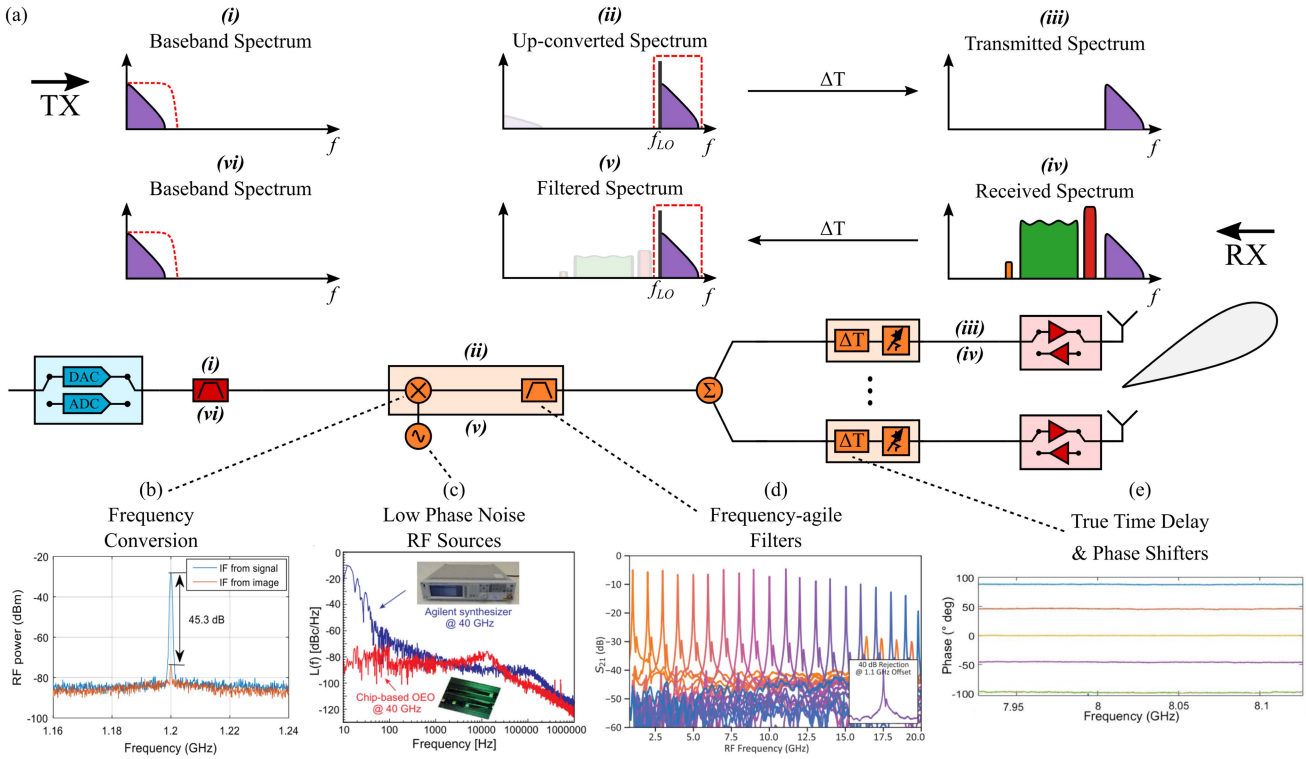

Fig. 3. (a) A typical analog beamforming architecture for a phased array antenna. In transmit mode, (i) a baseband signal from the DAC output is filtered, and (ii) converted to the PAA operating frequency before (iii) a delay and amplitude weighting is applied at each element before it is transmitted. In receive mode, (iv) a signal is received at each antenna element. Delay and amplitude weighting is applied at each element before (v) the spectrum is filtered to select a band of interest and converted to the baseband before (iv) the signal is filtered and undergoes analog to digital conversion. Essential microwave processing in this diagram has been demonstrated using on-chip Brillouin devices. Microwave processing and functional devices are shown in (b)–(e). (Fig. 3(b) from [72], © 2020, Optica Publishing Group. Fig. 3(c) from [71], © 2016, Optica Publishing Group. Fig. 3(d) from [69], © 2020, Optica Publishing Group. Fig. 3(e) from [77], © 2017, Optica Publishing Group.)

where d is the distance between adjacent elements in the PAA. The additional path Δx is caused by the applied phase shift, and is related to the operating wavelength, λ, by,

$$\frac{2\pi}{\Delta\phi} = \frac{\lambda}{\Delta x}. \tag{2}$$

Combining (1)–(2), and expressing the angle of the PAA beam in terms of the operating frequency, f, we get

$$\theta = \sin^{-1}\left(\frac{c\Delta\phi}{2\pi f d}\right), \tag{3}$$

where c is the speed of light. As can be seen from (3), one drawback of conventional beamforming using phase shifts is that the beam direction changes as a function of the transmitted frequency, referred to as beam squint [5]. Beam squint can be eliminated by introducing a TTD between elements to control the beam angle [81] by applying a linear phase shift to the RF signal of interest. The resultant delay, τ, is the derivative of the applied phase shift with respect to frequency [77], [78]. Substituting the relationship between the applied phase shift and frequency into (3), we find that the beam angle no longer directly depends on the PAA operating frequency [5]

$$\theta = \sin^{-1}\left(\frac{\tau c}{d}\right), \tag{4}$$

highlighting the advantages of using TTDs to implement beamforming in PAAs with wide signal bandwidths.

To understand the requirements for phase shifters and TTDs for beamforming, we solve for $\Delta\phi$ and τ in (3) and (4), respectively. Assuming that the PAA consists of N x N elements spaced by half the operating wavelength, $d = \lambda/2$, we find that the maximum phase shift and delay required is given by:

$$\Delta\phi_{\max} = \pi\,(N-1)\sin(\theta)\,, \tag{5}$$

$$\tau_{\max} = \frac{(N-1)\sin(\theta)}{2f}. \tag{6}$$

Using (5) and (6) we calculate the required phase and time delay to achieve steering over, $\theta = \pm 90°$. For PAAs based on phase shifts, a full 360° is required. For beam steering approaches based on TTDs, the required delay decreases with increasing frequency, and is less than 1 ns for 16 x 16 arrays above approximately 7.5 GHz, and only 150 ps at 50 GHz.

Fig. 3 illustrates a typical signal chain of a PAA, which includes beamforming hardware at each antenna element, frequency converters and local oscillators (LO) to interface between the PAA operating frequency and baseband, filters for analog signal conditioning, and baseband digital electronics; more information is provided in Refs [9], [82]. In transmit mode, a digital-to-analog converter (DAC) converts a digital input to an

analog baseband signal at point (i) in Fig. 3(a). This signal is filtered by a fixed frequency filter at the baseband to remove spurious content from the DAC. A local oscillator (LO) drives a mixer to convert the generated signal from the baseband to the PAA operating frequency, and is filtered again to remove spurious mixing terms at point (ii). The signal is then distributed to each antenna element of the PAA. Before transmission, delay and amplitude weightings are applied at each element to control the beam direction at point (iii).

The same concept applies for receive beamforming, but the signal chain is reversed, with an analog-to-digital converter (ADC) being used to digitise the received signal. In receive mode, the RF filter serves an additional purpose to select a signal of interest from the RF spectrum. Band-pass filtering may be required to select a particular band of interest, or a notch filter with fine frequency selectivity may be required to reject a particular interfering signal without attenuating adjacent signals at nearby frequencies.

Fig. 3(b)–(e) highlight demonstrations of Brillouin-based MWP processing devices that perform the key functions within a beamforming network, including frequency converters [72], low phase noise RF sources [71], filters [69], phase shifters [77] and TTDs [78]; we expand on these examples and conclude with a perspective on how these distinct functionalities can be combined onto a single photonic chip to enable element-level processing for PAAs.

III. Microwave Photonic Link Performance

MWP systems enable wide bandwidth processing of RF information with optical components using the canonical architecture shown in Fig. 4(a). An RF input signal is modulated onto a continuous-wave (CW) laser, where the RF spectrum is translated to the optical sidebands of the laser. This optical signal then undergoes processing in the optical domain before a photodetector (PD) converts it back to the RF domain through square law photodetection [83]. Although MWP systems enable operation over wide frequency ranges, they must also operate with low loss, low noise, and high linearity to ensure RF signal integrity is maintained [17].

The first metric discussed is the RF link gain, defined as the ratio of RF output power to RF input power. For MWP links using intensity modulation (IM) and direct photodetection, the link gain is given by [83]

$$g_{MWP} = \left(\frac{\pi r_{pd} R_L P_{opt} \sin(\phi_B)}{4 L V_{\pi_{RF}}} \right)^2, \tag{7}$$

where r_{pd} is the responsivity of the PD, R_L is the RF load resistance, P_{opt} is the laser output power, L is the loss of the MWP link, ϕ_B, and $V_{\pi_{RF}}$ are the bias angle and half-wave voltage of the E-O modulator, respectively.

The output noise power spectral density (PSD), p_n, of an MWP link is determined by three major contributions and is expressed as [21], [83]

$$p_n = (1 + g_{MWP}) kT + \frac{q r_{PD} I_{PD} R_L}{2} + \frac{10^{\frac{RIN}{10}} I_{PD}^2 R_L}{4}, \tag{8}$$

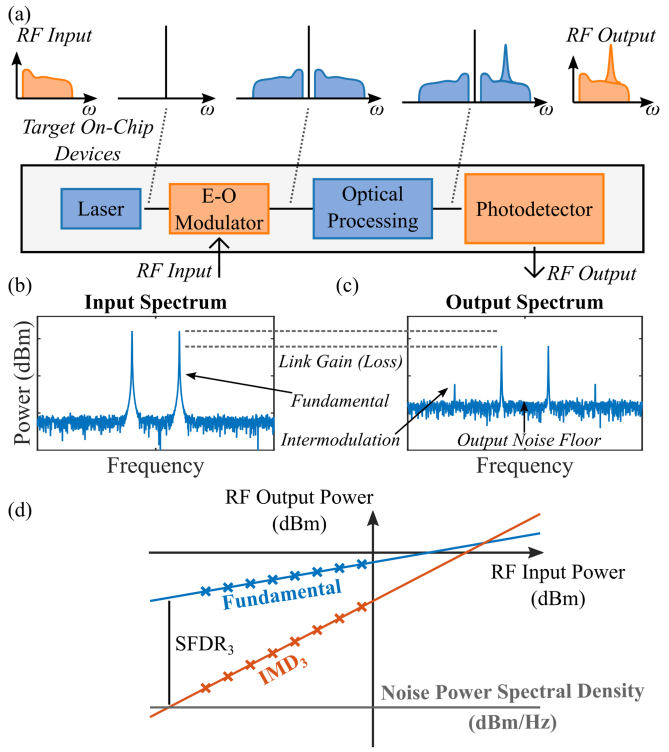

Fig. 4. (a) Simplified schematic of a microwave photonic link. An RF signal is modulated onto a continuous wave laser. The modulated signal is then processed optically before conversion back to the RF domain. (b) Typical input signal spectrum for the two tone test. (c) Typical output spectrum of MWP link for the two tone test. The RF link gain, third order intermodulation products (IMD_3), and noise floor are annotated. (d) Illustration of spurious free dynamic range. The fundamental tone output power, IMD_3 power, and noise power spectral density are labelled.

where q is the electronic charge, I_{PD} is the average photocurrent, RIN is the relative intensity noise of the optical signal at the PD, k is the Boltzmann constant, and T is the device temperature. The first term in (8) corresponds to thermal noise, the second term refers to the shot noise contribution, and the final term corresponds to the RIN noise contribution to the overall link noise. The noise PSD depends on the average photocurrent, which may be expressed as [83]

$$I_{PD} = \frac{r_{PD} P_{opt}}{2L} \left(1 - \cos(\phi_B)\right). \tag{9}$$

The key figure of merit to assess the noise degradation of an MWP link is the noise figure (NF), which quantifies the degradation of the signal-to-noise ratio (SNR) in an RF system and is given by [21], [83]

$$NF = PSD - G_{MWP} + 174, \tag{10}$$

where PSD is the measured noise power spectral density of the MWP link output, G_{MWP} is the MWP link gain in dB scale ($G_{MWP} = 10\log_{10}(g_{MWP})$), and 174 represents the thermal noise power spectral density at 290 Kelvin.

The third important metric of an MWP link is linearity. This must be considered to reduce the effect of unwanted harmonic

and intermodulation distortions, which are introduced by nonlinearities in the MWP link. The linearity of an MWP link is quantified by the spurious-free dynamic range (SFDR), and is measured using the two tone test [83], where two tones are input to the MWP link, as shown in Fig. 4(b). While many nonlinear mixing terms are created, the third order intermodulation products are of particular interest, as their frequencies are close to the frequency of the input tones [83], as shown in Fig. 4(c). SFDR_n is the power difference between the fundamental tone and the n^{th} order modulation products when their power is equal to the noise power in a 1 Hz bandwidth, as shown in Fig. 4(d). The SFDR_n corresponds to the maximum signal-to-noise ratio (SNR) that is achievable without the need to filter the n^{th} order distortion terms [29].

A number of optical processing techniques that improve the key performance metrics of MWP links have been demonstrated. For example, the NF of MWP links can be reduced using the technique known as low biasing [21], [83], where the bias angle is moved away from quadrature ($\phi_B = \pi/2$), towards the null bias point ($\phi_B = 0$). This may be understood by examining (7)–(10) and noting that the noise PSD decreases at a faster rate than the link gain decreases when the bias angle is reduced. Additional MWP link optimisation techniques include optimising the optical carrier to sideband ratio, whilst maintaining constant optical power at the PD to increase gain [69], [84], [85], reduce NF [86], and reduce third order non-linearity [85]. Additionally, optical processing has been used to ensure that RF intermodulation products destructively interfere. This reduces distortion and increases the SFDR of MWP links [87], [88]. Although optical amplifiers can be used to increase the RF link gain [89], they tend to be excessively noisy. Therefore, their location in the MWP link must be carefully considered to mitigate the excess noise they generate [90], [91].

IV. On-Chip SBS in Microwave Photonic Systems

A. Brillouin Scattering Overview

SBS occurs through a coherent interaction between optical pump and probe waves, and an acoustic wave [96], [97], [98]. This interaction can occur between counter-propagating optical waves referred to as backward Brillouin scattering, or between co-propagating waves referred to as forward Brillouin scattering [98]. A full theoretical treatment of SBS can be found in Refs. [54], [97], [98], [99], [100].

When the pump and probe have different frequencies, they create a travelling wave interference pattern. If the interference pattern travels at the acoustic velocity in the medium, and has sufficient intensity, it modifies the density of the waveguide through electrostriction and creates an acoustic wave [97], [98]. In turn, this leads to a change in refractive index through the photoelastic effect, and forms a travelling optical grating. This occurs when the pump and probe differ by the Brillouin frequency shift (BFS) in the medium, Ω_B. When incident upon this grating, the pump is Bragg reflected and Doppler shifted by frequency Ω_B, and constructively interferes with the probe. The increased probe power causes the intensity of the interference pattern to increase, which in turn amplifies the generated

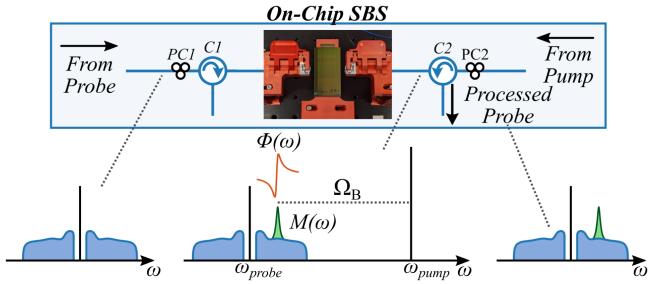

Fig. 5. Typical optical circuit used to implement backwards on-chip stimulated Brillouin scattering. C: Circulator, PC: Polarisation controller, Φ: Brillouin resonance phase response, M: Brillouin resonance magnitude response, Ω_B: Brillouin frequency shift.

acoustic wave and resonantly enhances the SBS process. A common schematic used to generate backwards SBS in MWP processors is shown in Fig. 5. The RF input is modulated on the optical probe, and is counterpropagated against the pump in the Brillouin medium. Circulators separate the counterpropagating pump from the probe before photodetection. The magnitude, M, and phase, Φ, of the SBS response are imparted on the optical signal and mapped into the RF domain. When Brillouin gain is stimulated by a pump with frequency ω_p, the magnitude and phase of the Brillouin response at frequency ω is given by [101]:

$$M(\omega) = \exp\left(G\frac{\Gamma_B^2}{4(\omega_p - \Omega_B - \omega)^2 + \Gamma_B^2}\right), \tag{11}$$

$$\Phi(\omega) = -G\Gamma_B\frac{(\omega_p - \Omega_B - \omega)}{4(\omega_p - \Omega_B - \omega)^2 + \Gamma_B^2}. \tag{12}$$

Γ_B is the linewidth of the Brillouin resonance and is inversely proportional to the phonon lifetime [102]. The parameter, G, is related to the intrinsic Brillouin gain coefficient, g_0, the acousto-optic effective area, A_{eff}, pump power, P_p, and the effective length of the Brillouin medium, L_{eff}, by [101]

$$G = \frac{g_0}{A_{eff}}P_pL_{eff}. \tag{13}$$

We note that it is often convenient to refer to the Brillouin gain coefficient, $G_{SBS} = g_0/A_{eff}$, which takes into account the intrinsic gain of the Brillouin medium and the acousto-optic effective area, which is determined by the waveguide geometry. The effective length is related to the physical waveguide length, L, and waveguide propagation loss, α, by $L_{eff} = \frac{1}{\alpha}(1 - e^{-\alpha L})$ [101].

B. Integrated Brillouin Platforms

Brillouin scattering has been induced in numerous chip-scale platforms [107] using three different strategies, as outlined in Fig. 6 and summarised in Table I, which details the key metrics used to characterise Brillouin platforms. The first approach is based on soft chalcogenide glass waveguides, which provides good confinement for both optical and acoustic modes because the speed of sound in the cladding is faster than in the core [54]. The second class of devices use silicon photonic waveguides, in which the acoustic mode is not strongly confined for traditional

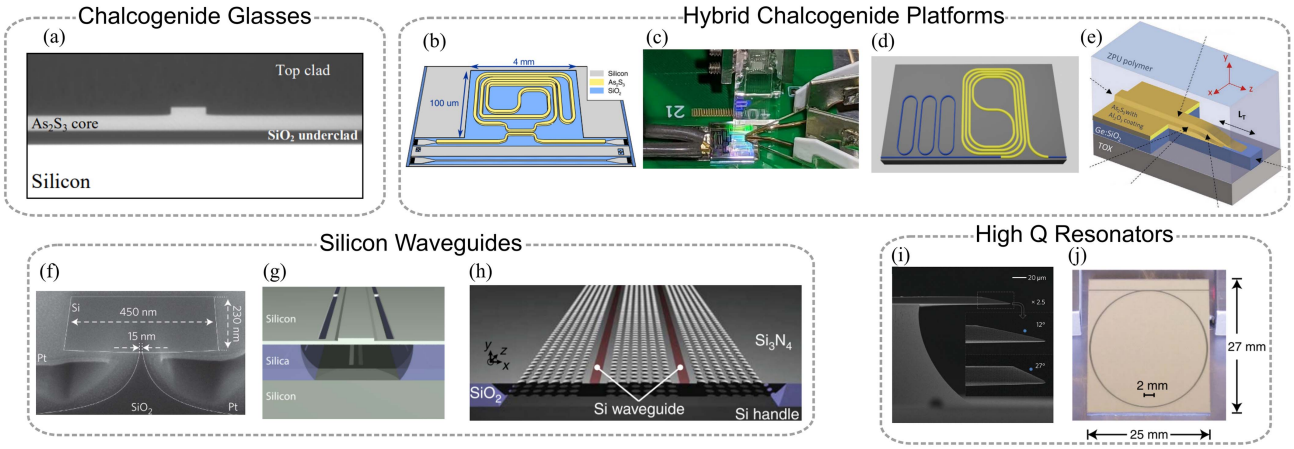

Fig. 6. Hardware platforms that have been used for on-chip Brillouin processing of microwave signals. (a) As_2S_3 chalcogenide waveguides. (b) Compact hybrid silicon and As_2S_3 devices. (c) Hybrid integrated SOI-As_2S_3 Brillouin processor currently under development. (d) Hybrid Si_3N_4 ring resonator and As_2S_3 Brillouin platform. (e) Vertically tapered Ge:SiO_2-As_2S_3 waveguides for reduced reflection interfaces. (f) Underetched silicon waveguide for forward Brillouin scattering. (g) Suspended silicon waveguide. (h) Photonic-Phononic Emit Receive (PPER) waveguides. (i) Silica micro-disk resonator. (j) Si_3N_4 micro-resonators. (Fig. 6(a) from [92], © 2007, Optica Publishing Group. Fig. 6(b) from [63], © 2017, Optica Publishing Group. Fig. 6(d) from [93]; licensed under a Creative Commons Attribution (CC BY) license. Fig. 6(e) from [94], © 2021 Wiley-VCH GmbH. Fig. 6(f) from [64], Reprinted by permission from Nature Publishing Group. Fig. 6(g) from [95], Reprinted by permission from Nature Publishing Group. Fig. 6(h) from [66]; licensed under a Creative Commons Attribution (CC BY) license. Fig. 6(i) from [68], Reprinted by permission from Nature Publishing Group. Fig. 6(j) from [67], Reprinted by permission from Nature Publishing Group.)

TABLE I
SUMMARY OF INTEGRATED BRILLOUIN PROCESSING PLATFORMS

Platform	Type	Brillouin Gain (dB)	G_{SBS} $\left(m^{-1}W^{-1}\right)$	L (cm)	α (dB/cm)	NL Loss (Y/N)	Ref
Chalcogenide As_2S_3 rib waveguides	B	52	500	23	0.5	N	[103]
Chalcogenide As_2S_3 strip waveguides	B	22.5	750	5.6	0.7	N	[63]
Chalcogenide $Ge_{25}Sb_{10}S_{65}$ strip waveguides	B	17.6	338	7	0.2	N	[104]
SOI underetched waveguides	F	0.6	3218	0.27	2.6	Y	[64]
SOI membrane suspended waveguides	F	6.9	1152	2.9	0.18	Y	[105]
SOI resonantly enhanced membrane suspended waveguide	F_{res}	30	380	1.5	0.13	Y	[106]
Si_3N_4 MRR	B_{res}	-	0.1	7.4	0.004	N	[67]

B - backward Brillouin scattering, F - forward Brillouin scattering, F_{res} - forward Brillouin scattering in a resonant device, B_{res} - backward Brillouin scattering in a resonant device. NL Loss - Nonlinear loss.

SOI rib and ridge waveguides [54]. The acoustic losses are reduced by suspending silicon waveguides above the substrate, so that it is essentially surrounded by air, thereby increasing mechanical isolation [64], [65], [66]. The third approach is the use of high Q factor resonant cavities, where long optical lifetimes enhance the generation of Brillouin gain, allowing for the use of materials with low Brillouin gain coefficients if they have low loss [67], [68].

The generation of backward SBS in As_2S_3 rib waveguides [62], which was the first demonstration of on-chip SBS, shown in Fig. 6(a), significantly reduced the interaction length required to generate SBS gain compared to previous fibre-based systems, and inspired the development of additional on-chip Brillouin microwave processing platforms based on chalcogenide glasses [104], [108]. Brillouin devices based on chalcogenide glasses combine strong acoustic confinement with negligible nonlinear loss, and have achieved more than 50 dB of Brillouin gain [103] using waveguides with lengths of a few centimeters that can be routed into compact and low-loss spirals. For example Morrison et al., achieved 22.5 dB of gain in an on-chip area less than 1 mm^2 [63], as shown in Table I.

Hybrid Brillouin platforms use multiple materials to enhance the functionality and performance of traditional As_2S_3 Brillouin devices. For example, integration of As_2S_3 waveguides with SOI platforms [63], shown in Fig. 6(b), combines the benefits of the large magnitudes of SBS gain offered by chalcogenide waveguides with the availability of passive and active components available in CMOS silicon photonics. Fig. 6(c) illustrates a typical SOI circuit that was fabricated by the IMEC foundry; this device aims to reduce the form factor of Brillouin processors by integrating As_2S_3 waveguides with active E-O components. Additionally, Si_3N_4 and As_2S_3 PICs [78], [93], as shown in Fig. 6(d), have been cascaded to enable MWP notch filters with reduced pump power requirements, and TTDs using separate carrier tuning; we expand on these devices in Section IV.

Although integration of multiple materials enhances functionality, the transitions between different materials must be carefully designed to minimise reflections of the Brillouin pump [94], which increases the spurious content in the RF output [93]. For example, Lai et al. measured a 4% reflection from the interface between lensed tip fibre and monolithic As_2S_3 chip [94], which is lower than the reflection at the interface between air and bulk As_2S_3 ($\approx$17%) owing to the use of lensed-fibres and the anti-reflection coating at the facet of the As_2S_3 chip [60]. Further reducing reflections of the Brillouin pump is desirable to minimise spurious content in the output

of the MWP link [93]. To reduce the reflection experienced by the Brillouin pump, a mode-matched and vertically tapered transition between As_2S_3 and germanosilicate waveguides [94] facilitated an adiabatic transition between materials, as shown in Fig. 6(e). This device achieved minimal optical back-reflections of only $\approx 0.04\%$ and promises to improve the performance of integrated Brillouin MWP processors [93].

Whereas SBS is typically observed in the backward direction in optical fibres and chalcogenide planar rib waveguides, it manifests in the forward direction for SOI devices. As mentioned, standard silicon waveguides lack intrinsic acoustic guidance, which causes acoustic modes to leak rapidly from the waveguide core, inhibiting the generation of Brillouin gain [109]. However, the phonon mode can be confined if the waveguide is suspended, thereby reducing acoustic losses and supporting the propagation of transverse acoustic waves, leading to the generation of forward Brillouin scattering [109]. As seen in Table I, silicon-based Brillouin platforms have large Brillouin gain coefficients and shorter interaction lengths than chalcogenide devices. However, as mentioned, they suffer from nonlinear loss at high pump powers, limiting the magnitude of Brillouin gain that can be generated [54]. Despite the aforementioned limited intrinsic acoustic guidance and nonlinear losses, SBS has been demonstrated in a number of SOI platforms [64], [65], [105].

Acoustic confinement has been achieved in an SOI platform using an underetched waveguide [64], as shown in Fig. 6(f). However, the magnitude of the generated Brillouin gain saturated at approximately 1 dB, limited by optical losses and free-carrier absorption at higher pump powers [64]. Subsequently, 30 dB of on-chip Brillouin gain was generated in an SOI platform using a Brillouin active membrane waveguide structure [106], shown in Fig. 6(g). However, the Brillouin-active waveguide was placed in an optical resonator to increase the magnitude of the generated Brillouin gain, limiting the functional bandwidth of the device.

One challenge faced by forward Brillouin devices is that the strong co-propagating pump must be filtered to avoid the generation of spurious terms caused by beating between the pump and probe at the PD [75]. The photonic-phononic emitter-receiver (PPER) structure demonstrated by Shin et al. [66] shown in Fig. 6(h), overcomes this challenge by placing the Brillouin pump and probe in spatially separated waveguides. In this approach, the pump is injected into the emitter waveguide and is modulated by an RF signal with a frequency that coincides with the Brillouin frequency shift (BFS). This generates an acoustic wave through forward Brillouin scattering [66], which modulates the phase of the optical signal in the adjacent, receiver waveguide through photoelastic coupling [66]. The signatures of acoustic waves with narrow linewidths as low as 2.4 MHz [110] have been observed, facilitating MWP filters with fine frequency resolution, as we discuss later in this section.

High Q optical resonators enable increased interaction times between the pump and probe, allowing for materials with low Brillouin gain coefficients to be used, and facilitates narrow linewidth optical tones that are suitable for generating stable RF signals. For example, silica wedge resonators are attractive for SBS-based processing due to their high Q and compact form factors [68], as shown in Fig. 6(i). Similarly, low-loss Si_3N_4 resonators, shown in Fig. 6(j), offer narrow Stokes linewidths below 1 Hz [67]. Despite their low Brillouin gain coefficient, shown in Table I, Si_3N_4 MRRs are able to generate Brillouin gain, owing to their extremely low losses.

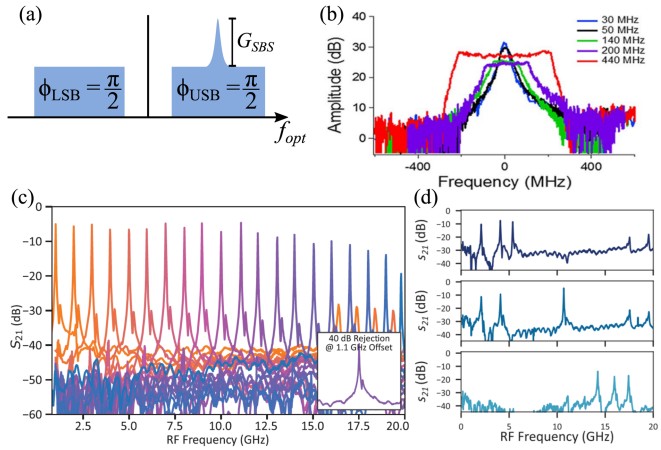

Fig. 7. Brillouin bandpass filters. (a) An example of an optical spectrum used to achieve bandpass filtering. (b) Passband reconfigurability by tailoring the on-chip Brillouin gain spectrum. (c)–(d) Bandpass filter response achieving 40 dB RF rejection ratio from 1–20 GHz. (Fig. 7(b) from [61], © 2016, Optica Publishing Group. Fig. 7(c)–(d) from [69], © 2020, Optica Publishing Group.)

C. Brillouin Microwave Photonic Filters

Microwave filters are essential components used to attenuate unwanted spurious or interfering signals in the RF spectrum [29]. MWP filters are required to exhibit wideband frequency tunability and fine frequency selectivity to attenuate unwanted signals whilst preserving nearby signals of interest. Therefore, Brillouin processing is particularly well suited for use in MWP filters as its fine spectral resolution enables narrow passbands or notches [17], [29].

The modulation scheme used in MWP filters has a significant impact on filter functionality and performance [29]. By altering the optical modulation scheme, both bandpass and notch filter functionalities can be realised [111]. Initial demonstrations of chip-based Brillouin MWP filters used single sideband modulation (SSB), and consequently were limited by a one-to-one spectral mapping of Brillouin gain to RF filter rejection ratio [111], [112], [113]. This is undesirable as it demands a considerable amount of pump power to generate large RF suppression [114]. For the remainder of this section, we outline approaches that combine advanced modulation formats [29], [111] with amplitude and phase control offered by SBS to enable high-performance MWP filters that do not require excessive Brillouin pump powers.

Bandpass filters enable transmission of a particular frequency range and are used to suppress out-of-band signals over a broad frequency range. In Brillouin-based processing systems, bandpass filters are realised using a modulation scheme that results in broadband destructive interference of output RF photocurrents in the absence of any Brillouin resonance. However,

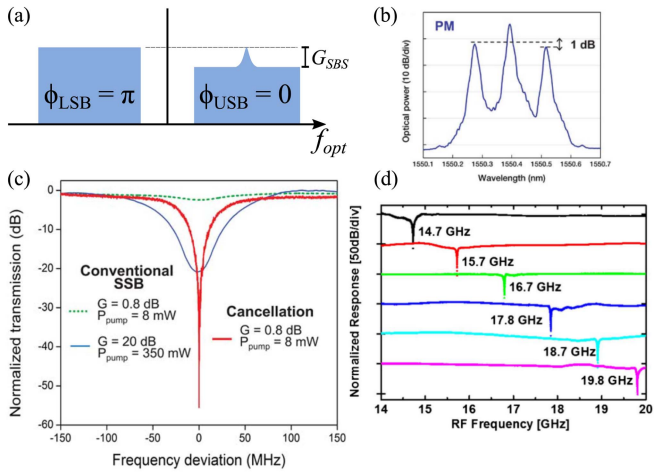

Fig. 8. Brillouin notch filters. (a) An example of an optical spectrum used for RF notch filtering. (b) Optical spectrum showing the amplitude difference between the upper and lower sideband before Brillouin gain is applied. (c) Demonstration of using only 1 dB of Brillouin gain to generate an RF notch with rejection exceeding 50 dB. (d) RF notch filter response that uses only 1 dB of SBS gain to achieve an RF rejection exceeding 50 dB. The notch frequency is tuned from 14.7–19.8 GHz. (Fig. 8(b)–(c) from [115], © 2015, Optica Publishing Group. Fig. 8(d) from [116], © 2015, Optica Publishing Group.)

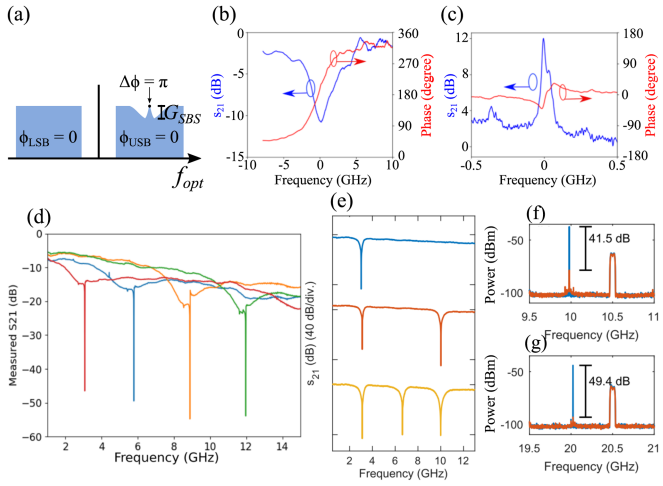

Fig. 9. RF notch filter created by cascading Brillouin resonances with ring resonators. (a) Optical spectrum used to achieve RF notch filter. (b) Measured phase and amplitude response of the over-coupled micro-ring resonator. (c) Measured phase and amplitude response of the Brillouin response. (d) Filtering using As_2S_3 ring resonators and As_2S_3 Brillouin waveguides. (e) Notch filtering utilising Brillouin processing in As_2S_3 waveguides and Si_3N_4 ring resonators for reduced notch bandwidth and notch frequency tunability. (f)–(g) Notch filtering demonstration achieving large out of band rejection. (Fig. 9(b)–(d) from [117]; licensed under a Creative Commons Attribution (CC BY) license. Fig. 9(e)–(g) from [93]; licensed under a Creative Commons Attribution (CC BY) license.)

when SBS is applied to one sideband, it breaks the condition for destructive interference and forms a narrow passband [69], [111]. Fig. 7(a) depicts one modulation scheme that provides this functionality [69], [85]. Fig. 7(b) highlights how the parametric generation of Brillouin gain enables reconfigurable MWP filters, demonstrating passband bandwidth broadening from 30 MHz to 440 MHz [61], by broadening the Brillouin pump spectrum using an E-O modulator. In this demonstration, the probe was phase modulated, which led to destructive interference of RF photocurrents outside the Brillouin resonance [111] and increased the MWP filter RF rejection ratio compared to MWP filters based on SSB modulation. Filters with widely tunable passbands from 1–20 GHz have been demonstrated by changing the relative frequency between the pump and probe, shown in Fig. 7(c). Rejection ratios exceeding 40 dB are achieved using only 14 dB of on-chip SBS gain [69]. Multiple passbands are generated by using additional Brillouin pump tones, shown in Fig. 7(d).

Notch filters are used to attenuate unwanted signals at a specific frequency. RF notches are formed by Brillouin-based devices, which use the SBS resonance to ensure RF photocurrents destructively interfere [115], [116]. One way to achieve this is shown in Fig. 8(a), where the upper and lower sidebands of the probe are π out of phase and mismatched in amplitude by the magnitude of applied Brillouin gain [115], [116]. At the Brillouin resonant frequency, the upper and lower sideband are equal in amplitude, but π out of phase, and therefore their RF photocurrent contributions destructively interfere upon photodetection. Outside the Brillouin resonance, the upper and lower sidebands are not equal and therefore do not cancel. Fig. 8(b) shows the modulation scheme used by Marpaung et al. that formed the basis of a notch filter using 1 dB of Brillouin gain. The filter demonstrated notch depths exceeding 50 dB [115], shown in Fig. 8(c). Similarly, Casas-Bedoya et al. required only 1 dB of forward Brillouin gain to demonstrate a widely tunable filter response using a SOI platform, as shown in Fig. 8(d) [116]. One advantage of the modulation scheme in Fig. 8(a) is that the pump power required to form a notch is greatly reduced when compared with non-interferometric approaches. However, the broadband π phase difference between upper and lower sidebands creates an RF gain penalty when the upper and lower photocurrent contributions are added.

Combining on-chip linear optical devices, for example MRRs, with Brillouin processing [93], [117] is an attractive method to implement an MWP notch filter without a gain penalty in the passband. In this notch filter scheme, an over-coupled MRR imparts a spectrally localised π phase shift to the upper sideband at its resonant frequency. Brillouin gain is then applied at the MRR central frequency to overcome the reduction in signal amplitude caused by the MRR resonance. The upper sideband therefore experiences a localised π phase shift with an unchanged amplitude, while the lower sideband is equal in amplitude and has unchanged phase, as shown in Fig. 9(a). An RF notch is formed upon photodetection as the photocurrent contributions from upper and lower sidebands are equal in magnitude at the overlapped MRR and SBS resonant frequency, but π out of phase.

The first demonstration of this concept used optical fibre as the SBS medium [118] and was subsequently demonstrated in a monolithically integrated As_2S_3 platform [117]. The measured magnitude and phase response of the As_2S_3 MRR is shown in Fig. 9(b), where a π phase shift is observed at the MRR resonance. The SBS gain response in As_2S_3 waveguides is shown in

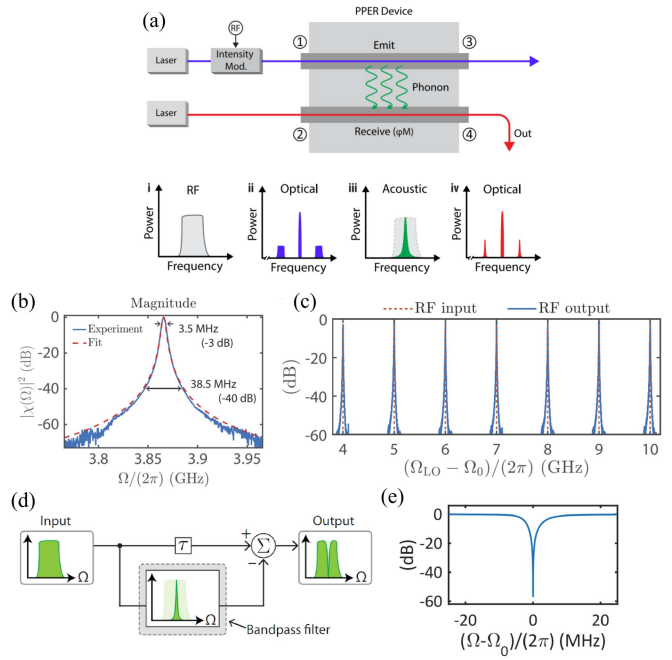

Fig. 10. (a) Schematic outlining the generation of forward SBS in PPER waveguides. (b) Bandpass filter response using PPER waveguides. (c) Tunable filter responses using PPER waveguides to create a bandpass filter. (d) Architecture for interference-based notch filter using PPER waveguides. (e) RF notch filter response using PPER device and RF interference scheme. (Fig. 10(a) from [119], © 2018, IEEE. Fig. 10(b)–(c) from [120]; licensed under a Creative Commons Attribution (CC BY) license. Fig. 10(d)–(e) from [110]; licensed under a Creative Commons Attribution (CC BY) license.)

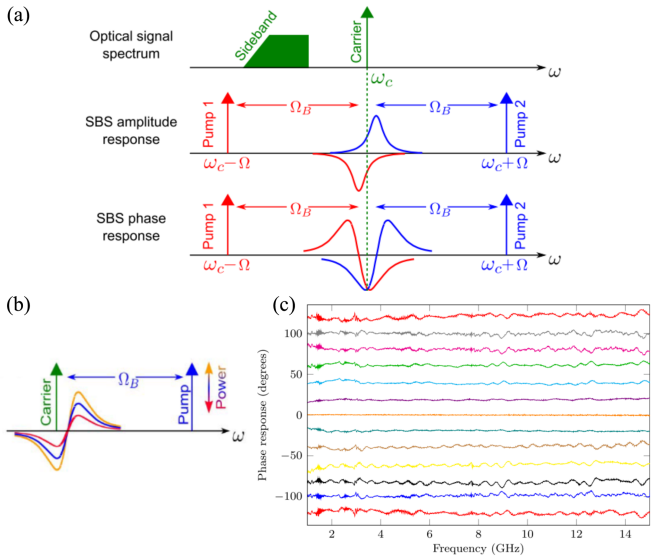

Fig. 11. RF phase shifter using on-chip SBS (a) Operating principle. Brillouin gain and loss resonances are aligned such that the maximum phase excursion is applied to the optical carrier (b) The RF phase shift is tuned by changing the Brillouin pump power. (c) Measured broadband 240° phase shift. (Figures from [74], © 2014, Optica Publishing Group.)

Fig. 9(c), which does not impart any phase shift at its resonant frequency. The RF filter response using the monolithically integrated As_2S_3 platform exhibits tunable notch frequencies by changing the probe frequency relative to the MRR resonance, as shown in Fig. 9(d). Propagation losses in the As_2S_3 MRR limits the 3-dB bandwidth of the RF notch to 3 GHz [117]. The key to the passband link gain improvement offered by this scheme is attributed to the fact that the SBS and MRR responses do not impart a phase or amplitude change outside of their resonance, as seen in Fig 9(b)–(c). This results in constructive interference of RF photocurrents in the passband from the in-phase IM sidebands, and is not the case for the Brillouin-based notch filters discussed above, where the sidebands are out of phase with each other and do not sum constructively in the passband which increases RF losses [115], [116].

More recently, an MWP filter scheme was demonstrated that combined tunable and narrow linewidth Si_3N_4 MRRs cascaded with As_2S_3 waveguides to enhance functionality and reduce the 3-dB RF notch bandwidth from 3 GHz to 500 MHz [93]. Up to three low-loss Si_3N_4 MRRs were overlapped with three Brillouin gain resonances to enable an MWP filter with three independently controllable notches, as shown in Fig. 9(e). The filter was demonstrated to suppress undesired signals by up to 49.4 dB, which were 500 MHz from a signal of interest, shown in Fig. 9(f)–(g).

PPER waveguides, as outlined in Section IV, offer an alternate approach for implementing MWP bandpass [120], [121] and notch filters [110], which circumvent the need to filter the high-power Brillouin pump, as demonstrated by Gertler et al. An MWP filter with a passband centred at the BFS, Ω_B, is realised by encoding the RF input signal onto the pump laser through intensity modulation [120], as shown in Fig. 10(a). If the RF input contains a signal with frequency Ω_B, an acoustic wave is generated, which modulates the phase of the CW laser in the adjacent receiver waveguide. An optical bandpass filter removes one sideband of the phase modulated signal so that when this filtered optical signal is converted to the electrical domain, the RF signal is present in the device output. However, input RF signals that do not coincide with the BFS do not induce an acoustic wave, and are therefore suppressed by the MWP filter.

Fig. 10(b) shows the bandpass RF filter response of the fabricated device with a BFS of 3.86 GHz and 3-dB bandwidth of 3.5 MHz [122]. The passband frequency is changed by using phase modulation to encode the RF information onto the pump, and introducing a second laser to the pump spectrum, which has a frequency offset from the original pump laser [120]. Tuning of the passband frequency is shown in Fig. 10(c). MWP notch filters have been demonstrated using PPER waveguides [110], as shown in 10(d). In this scheme, the PPER waveguides select a narrow region of the RF spectrum, which is subsequently subtracted from the original input signal, forming a notch filter through destructive interference. Using this technique, an RF notch filter, as shown in Fig. 10(e), with rejection of up to 57 dB has been observed with bandwidth as narrow as 2.7 MHz [110].

D. Brillouin Phase Shifters

Phase shifters and TTDs are essential components responsible for beamforming in PAAs. The ideal RF phase shifter provides

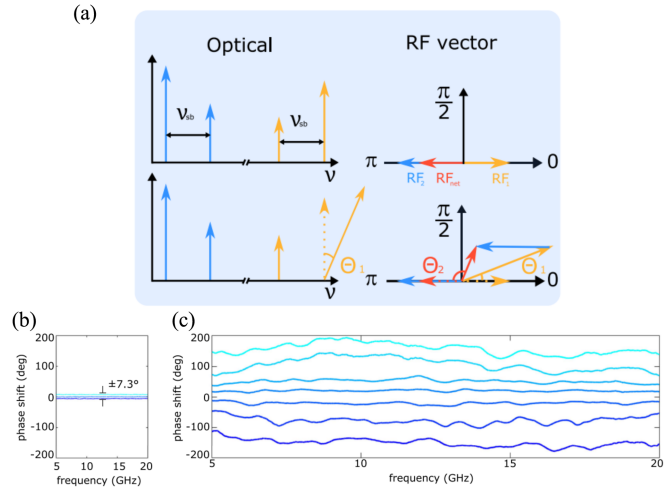

Fig. 12. SBS-based phase shifter using RF interference scheme for phase amplification. (a) Operating principle. (b) Raw Brillouin phase response showing only ±7.3° phase shift. (c) Amplified phase response obtaining a full 360° phase shift from the raw response in (b). (Figures from [75], © 2019, Optica Publishing Group.)

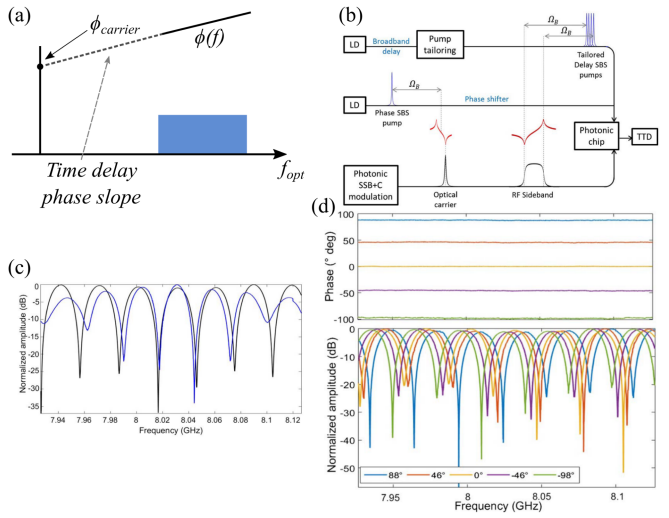

Fig. 13. SBS-based true time delay using separate carrier tuning (a) Operating principle. (b) Experimental setup. (c) The difference in FSR of two tap filter corresponds to a delay of 4 ns. (d) A phase shift applied to the optical carrier changes the null location of the interference pattern. (Fig. 13(b)–(d) from [77], © 2017, Optica Publishing Group.)

a 360° tunable phase shift with flat amplitude response over a wide RF frequency range. Brillouin-based MWP phase shifters typically use SSB modulation and apply a phase shift to the optical carrier from the phase shift associated with the Brillouin resonance, given by (12). This phase shift translates to a broadband phase shift in the RF output [90].

Pagani et al. demonstrated a MWP phase shifter using on-chip SBS [74] by applying equal amounts of Brillouin gain and loss to impart a phase shift to the optical carrier with minimal amplitude fluctuations, as shown in Fig. 11(a). The generated RF phase shift was tuned by changing the Brillouin pump powers, as shown in Fig. 11(b). A continuous RF phase shift of 240° was observed, shown in Fig. 11(c), while keeping RF power fluctuations within only ± 1.5 dB. Although good performance was demonstrated, achieving 360° phase tunability, which is required for beam steering in PAAs, demands more than 50 dB of Brillouin gain, leading to excessively large optical pump power [75].

RF interferometric techniques can be harnessed to provide a full 360° phase shift, without requiring high Brillouin pump powers; this approach uses RF vector addition to amplify the RF phase shift generated from an optical phase shift [123]. This scheme, summarised in Fig. 12(a), consists of two RF photocurrent contributions. The first contribution, RF_1, is assigned a phase of 0. The second, RF_2, has a relative phase shift of π and is used for interferometric phase amplification. The output of this system, RF_{net}, is given by the vector summation of these two signals. When RF_1 and RF_2 are added, the overall phase shift, Θ_2, is larger than the optical phase shift, Θ_1, applied to RF_1, at the expense of a reduced RF link gain [78]. The phase enhancement factor is defined as the ratio of the enhanced phase shift to the raw phase shift [75].

Fig. 12(b) shows the un-enhanced ±7.3° phase shift over the RF frequency range 5-20 GHz generated from 2 dB of Brillouin gain using suspended silicon waveguides [75]. When the phase is amplified by the interferometric phase enhancement technique, a 360° phase shift is achieved using an enhancement factor of 25, as shown in Fig. 12(c). Subsequently, this scheme was demonstrated using As_2S_3 waveguides and a 360° phase shift was generated up to 20 GHz using only 19 dBm of coupled on-chip pump power [76], compared to a total of 27 dBm on-chip pump power required to generate the 240° phase shift [74] in a similar As_2S_3 platform. The demonstrations of interferometric phase enhancement highlight the primary benefit of this interferometric technique, enabling 360° RF phase shifts while using minimal amounts of Brillouin gain.

E. Brillouin True Time Delays

While RF phase shifters may be used to implement analog beamforming for narrowband signals, beam squint occurs as the signal bandwidth increases [124]. TTDs are therefore preferred for wideband signals as they eliminate beam squint. MWP systems generate TTDs by applying a linear dispersive phase slope over a frequency range that includes the optical carrier and modulated sideband. However, this requires a delay to be applied from the optical carrier to the highest frequency component on the RF sideband, which is greater than the bandwidth of most photonic components [125]. Alternatively, the separate carrier tuning (SCT) [126] method is well suited to generate TTDs for MWP applications and is implemented by applying a linear phase slope, such as SBS slow-light effects [102], [127], [128], [129], to an optical sideband and separately applying the appropriate phase shift to the optical carrier, as shown in Fig. 13(a).

The SCT method has been demonstrated using chip-based Brillouin devices by Aryanfar et al. [77], shown in Fig. 13(b). The TTD was verified using a two-tap filter, which is an unbalanced interferometer with one arm containing the TTD and the other maintaining constant delay. The change of free spectral range (FSR) of the interferometer in Fig. 13(c) corresponds to a

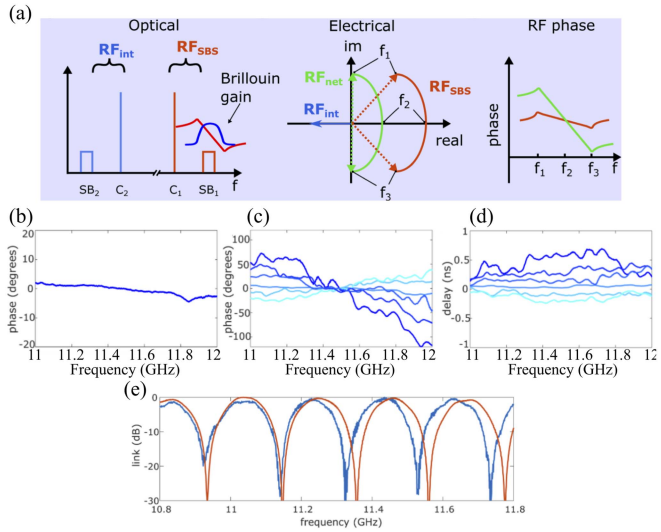

Fig. 14. SBS-based true time delay enhancement using an RF interferometric technique. (a) Operating principle of interferometric true time delay (b) Raw Brillouin phase response over 1 GHz. (c) Enhanced phase response over 1 GHz. (d) Enhanced time delay over 1 GHz. (e) Two tap filter, showing change of free spectral range due to the imposed time delay. (Figures from [78], © 2020, Optica Publishing Group.)

delay of 4 ns over a 100 MHz bandwidth [77]. The phase shift applied to the optical carrier is indicated in Fig. 13(d) by the change of the null frequency in the interferometer pattern.

The delay generated by an MWP system can be enhanced through interferometric techniques [78] using a similar principle as the phase enhancement technique for MWP phase shifters. Liu et al. [90] demonstrated dispersive phase slope enhancement which increased Brillouin slow light delay, but lacked carrier phase tunability to meet the SCT condition for generating a TTD. McKay et al. demonstrated TTD enhancement using the SCT method [78], shown in Fig. 14(a). In this approach, two widely separated optical carriers, C_1 and C_2, are used and both undergo single sideband modulation. However, the sidebands of each carrier are π out of phase relative to each other. Broadband Brillouin gain is applied to the sideband of C_1, which causes a dispersive phase slope. A Si_3N_4 MRR applies the appropriate phase shift to C_1 to implement SCT, and a second MRR applies the same phase shift to C_2 to ensure that C_1 and C_2 maintain a π phase offset. The overall phase shift is increased through the summation of the output photocurrents RF_{SBS} and RF_{int}, which originate from the two optical carriers.

Fig. 14(b) shows the raw phase slope from the Brillouin resonance over a 1 GHz bandwidth, between 11 and 12 GHz. Fig. 14(c) shows the phase slope created when using enhancement factors of up to 30. The corresponding delay for each phase slope in Fig. 14(c) is shown in Fig. 14(d). We note that fluctuations in the phase and delay responses are amplified due to the phase enhancement scheme, and can in principle be reduced by finely tailoring the Brillouin gain spectrum to achieve the desired response [78]. Fig. 14(e) shows the two tap-filter response with and without the TTD applied. The change to the FSR corresponds to a delay of 330 ps [78], which is suitable for

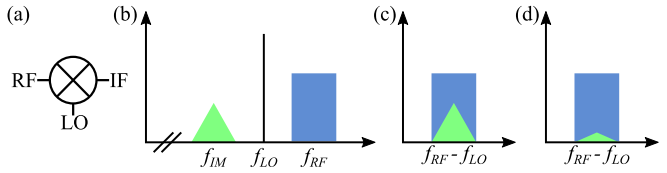

Fig. 15. (a) Schematic symbol for an RF mixer. (b) Example spectrum to be converted in frequency. (c) Downconverted spectrum without image rejection. (d) Downconverted spectrum with image rejection. Note the signal at the image frequency is attenuated.

beam-steering applications for a 16x16 array operating in the K-band and above, as outlined in Section II.

If even larger delays are required for PAAs with more elements Brillouin-based light storage [130], quasi-light storage [131], and Brillouin dynamic grating based approaches [132], [133], [134] have been shown to achieve larger delay-bandwidth products compared to the Brillouin slow-light based approaches outlined above. However, so far those techniques have only been shown for optical signals and they still have to be demonstrated in an MWP link and only the former has been shown in an integrated platform [130]. Besides the large fractional delay achieved using Brillouin light storage it has been shown that the strict phase-matching condition between optical and acoustic waves in the Brillouin process can be used to induce non-reciprocal delays [135] which might open possibilities for novel processing methods in PAAs.

Alternatively, recent approaches utilise the polarisation dependence of Brillouin gain in both spun birefringent [136], and standard single mode [137] fibres to introduce narrow sub-MHz spectral dips within the Brillouin gain resonance. The spectral dip gives rise to a steep phase slope, which could form the basis of an MWP phase shifter or TTD with the potential to reduce the link gain penalty compared to the phase and delay enhancement techniques outlined above. Initial demonstrations of polarisation pulling using SBS in As_2S_3 waveguides by Athanasios et al. [138] highlights possibilities of implementing such optical processing techniques on PICs in a compact form factor.

F. Brillouin Frequency Converters

RF frequency converters, often referred to as mixers, are used to convert between RF and a lower intermediate frequency (IF) [72], which is a critical function in PAAs. A mixer is a three port device, as shown in Fig. 15(a), where the frequency of the input RF signal is translated according to its difference in frequency from a second CW input tone, referred to as a local oscillator (LO). When downconverting a spectrum that contains a desired signal at frequency, f_{RF}, and a signal equally spaced but on the other side of the LO at frequency, f_{IM}, they are both converted to the same IF frequency, as shown in Fig. 15(b)–(c). The undesired signal in the IF spectrum is referred to as an image and causes distortion. The process of suppressing the image signal in the IF spectrum is referred to as image rejection [139], and is depicted in Fig. 15(d).

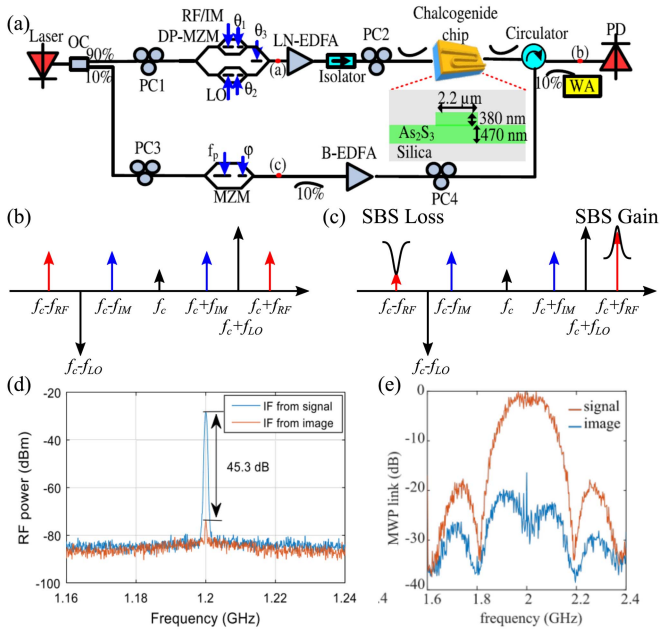

Fig. 16. Brillouin-based RF frequency converters. (a) Experimental setup for Brillouin-based image rejection mixer. (b) Optical spectrum without Brillouin processing. (c) Optical spectrum after Brillouin processing. Gain and loss are applied to the RF signal of interest on the upper and lower sideband, respectively. (d) The IF spectrum of a narrowband Brillouin mixer. An image rejection of 45.3 dB was achieved. (g) The IF spectrum of a broadband Brillouin downconverter showing 16 dB of image rejection from over a 400 MHz band. (Fig. 16(a, d) from [72], © 2020, Optica Publishing Group. Fig. 16(e) from [73], © 2021, IEEE.)

Brillouin-based MWP mixers inherently perform image rejection by ensuring that the output photocurrents destructively interfere in the absence of a Brillouin resonance. Zhu et al. demonstrated a chip-based SBS image-rejection mixer [72], which utilised a dual-parallel Mach-Zehnder modulator (DP-MZM) by placing the RF input on the top sub-MZM and the LO input on the lower sub-MZM, shown in Fig. 16(a). The DPMZM was biased to ensure destructive interference outside the Brillouin resonance, as shown in Fig. 16(b). Frequency conversion occurs when Brillouin gain is applied to the signal of interest on the upper sideband, and SBS loss is applied to the signal of interest on the lower sideband, as shown in Fig. 16(c). When SBS gain and loss are applied to the signals of interest, the photocurrent amplitudes are unequal and cause an output to form. An image rejection of 45.3 dB [72] was achieved using 15.1 dB of SBS gain and 13.3 dB of SBS loss, shown in Fig. 16(d). This system exhibited a conversion gain of −9 dB over the 3.2–13.2 GHz frequency range [72]. Although this demonstration provides low-loss conversion and deep image rejection, it only supported frequency conversion of narrowband signals. However, broadband image-rejection frequency conversion is required for compatibility with modern PAAs. McKay et al. demonstrated broadband image rejection downconversion using on-chip SBS by modulating the Brillouin pump over a broad bandwidth. In doing so, broadband image rejection of 28 dB and 16 dB was achieved over 100 MHz and 400 MHz, respectively [73], as shown in 16(e).

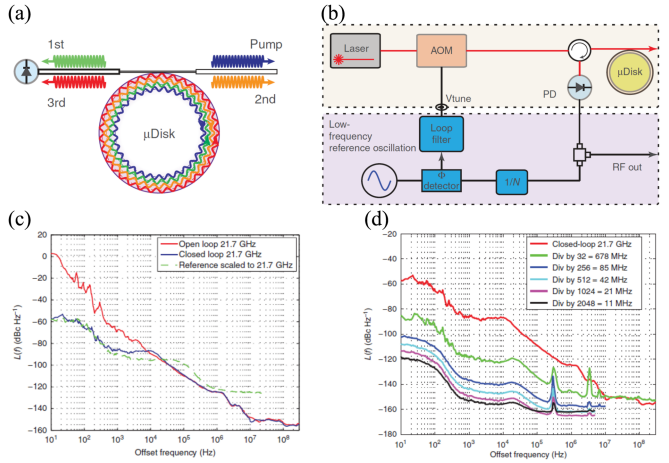

Fig. 17. Brillouin-based RF source using silica resonator. (a) Principle of Brillouin RF source. An optical pump generates higher-order Brillouin responses, forming the tones used to create the RF signal. (b) Simplified schematic of Brillouin RF source. (c) Single-sided phase noise of RF source with and without closed loop operation. (d) Phase noise improvements to the 21.7 GHz output when its frequency is divided. (Figures from [70], licensed under a Creative Commons Attribution (CC BY) license.)

G. Brillouin Radio Frequency Sources

RF sources are essential components in the PAA, and when used in conjunction with an MWP frequency converter, enable PAAs with widely tunable central frequencies. RF sources with low phase noise are critical in wireless communication [140] and radar [71], [141] systems. However, RF frequency synthesizers typically generate an output that is up-converted from a stable, low frequency electronic source. The up-conversion process increases the phase noise by a factor $20\log_{10}(N)$ [70] when the frequency is multiplied by a factor of N. In practice, the phase noise is increased by additional noise from RF amplification stages [142]. Conversely, MWP-based RF sources directly generate outputs at radio frequencies by heterodyning two, or more optical tones. Brillouin laser cavities have been used to enable significant reductions to the linewidth, in addition to close-in frequency noise and RIN noise [67] of optical tones. Brillouin lasers have formed the basis of RF sources that achieve phase noise comparable to [70], or lower than the phase noise of high-performance RF microwave sources [143]. Additionally, photonic-based approaches have the distinct advantage of being able to generate RF tones over wide frequency ranges [71], [143].

Li et al. used Brillouin lasing in a high Q silica disk resonator [68] as the basis of a low phase noise RF source [70]. The main advantage of this scheme is that common mode jitter is reduced because the Brillouin laser lines share the same optical path [70], reducing the phase noise of the RF output. The operating principle of this device is shown in Fig. 17(a), where cascaded Stokes waves are generated in the silica disk. The first and third order tones co-propagate and are separated in frequency by twice the BFS, 21.7 GHz [70]. An RF signal with a frequency of 21.7 GHz is formed when both tones mix at a PD. Although the close-in phase noise (<10 kHz) of this device is relatively large when free-running, it is reduced

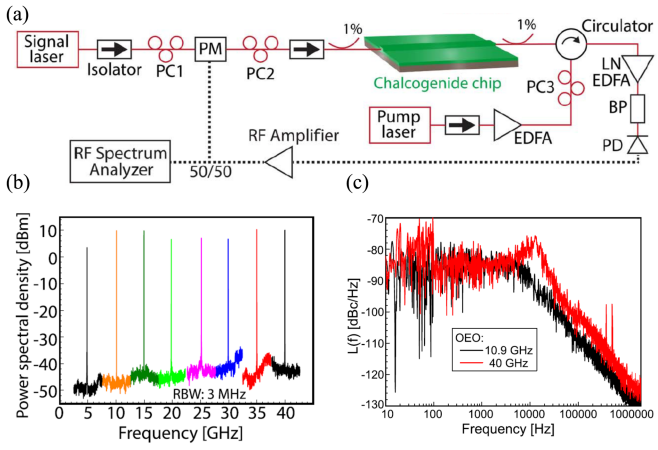

Fig. 18. Chip-based Brillouin optoelectronic oscillator (OEO). (a) Experimental setup for Brillouin based OEO. (b) Wideband tunability of SBS OEO. Images taken from [71]. (c) Phase noise for generated signals at 10.9 GHz and 40 GHz. (Figures from [71], © 2016, Optica Publishing Group.)

using closed-loop control to form a phase-locked loop, as shown in Fig. 17(b). The feedback loop allows for the use of a stable low-frequency quartz oscillator as a frequency reference [70], which improves the output phase noise, shown in Fig. 17(c). A low white-phase-noise floor of −160 dBc/Hz was obtained [70]. When the output frequency is divided, the phase noise improves, as shown in Fig. 17(d). We note that high Q Si_3N_4 MRRs, demonstrated by Gundavarapu et al., have been used to form an RF source through cascaded Brillouin generation. This approach offers narrow Stokes linewidths of only 0.7 Hz [67], and is an attractive method to generate low phase noise RF signals. It is desirable to generate microwaves with continuous frequency tunability for use in PAAs, however, the frequency of the RF output is limited to discrete frequencies determined by the BFS [67], [70].

Li et al. extended on the work presented in [70] by demonstrating a continuously tunable RF source using two lasers locked to distinct modes of a common Brillouin laser cavity [143]. A reduction in phase noise was achieved through optical frequency division.

Optoelectronic oscillators (OEOs) [144] are an alternate method to generate low phase noise RF signals. However, most OEOs rely on a narrowband filter to select one cavity mode, which are not widely tunable if implemented using traditional electronic methods [71]. On-chip SBS enables widely tunable filtering functionality, and has been used as a widely tunable MWP filter to select the desired OEO loop mode and enable wideband RF signal generation, as shown in Fig. 18(a) [71]. In this approach, Brillouin gain amplifies one cavity mode to create phase-intensity modulation conversion and sustain an oscillation. Using this technique, an RF tone was synthesised with frequency up to 40 GHz, as shown in Fig. 18(b). The advantage of optically generating microwave tones over a wide frequency range is highlighted in Fig. 18(c), where signals at 10.9 GHz and 40 GHz have similar phase noise.

H. Non-Reciprocal Devices

Non-reciprocal components are key to on-chip photonic processors, as they protect optical components from back-reflected light [145], which is particularly important for backward Brillouin photonic devices in which counterpropagating pump and probe signals are required [54]. Optical devices traditionally achieve non-reciprocity using magneto-optical materials which induce a non-reciprocal Faraday rotation [146]. While chip-scale isolators and circulators using magneto-optic garnets [147] have demonstrated large 30 dB isolation over a wide 16 nm 10-dB bandwidth [148], these devices are challenging to integrate into PICs [149].

Non-reciprocity requires the breaking of time reversal symmetry, which can be implemented using SBS [150]. Acousto-optic non-reciprocal devices rely on phase matched optical mode conversions that occur for optical waves travelling in one direction but not the other [150], [151]. Chip-based demonstrations of optical non-reciprocity have utilised resonant structures [149], [152], which limited the usable bandwidth, or required suspended waveguides to increase acoustic guidance [95], [153], which increased fabrication complexity. On-chip non-reciprocity has been achieved without the use of resonant structures [38], [154]. For example, Kittlaus et al. recently demonstrated an electrically induced acoustic wave using standard silicon waveguides and on-chip mode multiplexers to facilitate non-reciprocal intermodal acousto-optic scattering [155]. This device achieved over 16 dB of optical isolation over a 100 GHz bandwidth without the use of an optical cavity [155].

An alternate approach introduced by Liu et al. [156] avoids the requirement for a non-reciprocal element by exploiting backward inter-modal Brillouin scattering (BIBS) in combination with passive mode-selective filters. However, less than 1 dB of BIBS gain was observed [156]. Therefore, further developments to this platform are required to increase the magnitude of BIBS gain generated to make this platform suitable for MWP processing.

V. Outlook for Integrated Brillouin Phased Array Antenna Systems

The long-term goal of MWP is a fully-integrated processor with enhanced functionality that supports signals with wide bandwidths over wide frequency ranges. This system must also meet the demanding performance specifications of real-world RF systems in terms of noise figure, linearity and insertion loss. This section outlines technological advances that are required to realise a high-performance and fully-integrated Brillouin-based MWP processor that incorporates multiple passive and active photonic components to enable key PAA processing functionalities, including beamforming elements based on Brillouin TTD, and image rejection frequency converters to interface between the RF operating frequency and the baseband.

A. Architecture of Brillouin-Based Phased Array

A potential architecture of a PAA using fully-integrated MWP processors is shown in Fig. 19(a). To simplify the discussion

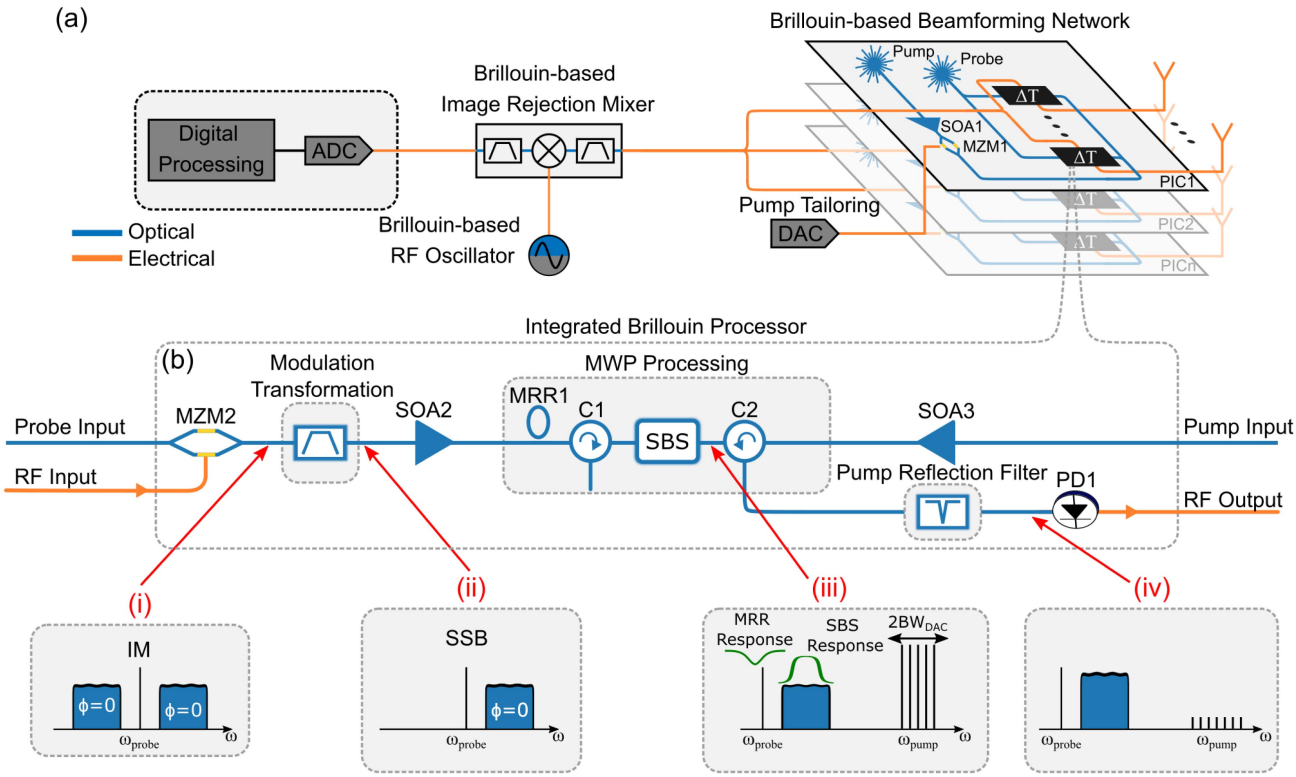

Fig. 19. Phased array antenna enabled by on-chip Brillouin processing. (a) Optical signal distribution scheme for MWP-based PAA processing. (b) Schematic for proposed multi-purpose SBS-enabled MWP beamformer. (i) An RF signal is modulated onto the probe laser. (ii) A modulation transformer generates the required modulation format. (iii) On-chip Brillouin and passive processing. (iv) Processed optical signal with filtered pump reflection. L: laser, MZM: Mach-Zehnder Modulator, LO: local oscillator, BPF: bandpass filter, DAC: digital to analog converter, SOA: semiconductor optical amplifier, SW: switch, MRR: micro-ring resonator, ODL: optical delay line, C: circulator, PD: photodetector.

without loss of generality, we discuss the PAA operating in receive mode. The proposed architecture consists of a Brillouin beamforming network with a PIC at each row of the PAA, where integrated Brillouin processors implement TTD beamforming at each antenna element. Chip-based pump and probe lasers are routed to each integrated Brillouin processor and the spectrum of each pump is broadened by a DAC which drives MZM1. The signal from each integrated Brillouin processor is combined and converted to the baseband using a Brillouin-based image rejection mixer driven by a low-noise Brillouin-based oscillator. This ensures signals outside of the band interest are attenuated through destructive interference [72], [73], essentially acting as a MWP filter cascaded with a frequency converter.

The core components of the integrated Brillouin processor are highlighted in Fig. 19(b), which works as follows; an input RF signal is modulated onto the optical carrier by MZM2 at (i), a modulation transformer [157], [158] generates the required modulation format at (ii), on-chip optical amplifiers set the pump and probe power as required before the probe undergoes Brillouin processing at (iii), an optical notch filter suppresses reflections of the Brillouin pump at (iv). Reflections are primarily caused by index changes between different materials and can be greatly reduced in an appropriately designed integrated platform, compared to systems that rely on a combination of chip-scale and fibre components [94]. Finally, the signal is converted back to the RF domain. This architecture can be extended to enable phase or delay amplification, as outlined in Section IV, by adding additional core components outlined in Fig. 19(b).

B. *Integrated Platforms and RF Link Performance*

Integration of multiple materials is key to realising the integrated Brillouin processor in Fig. 19, as no single material platform provides all the necessary functionalities [159]. The integrated Brillouin processor requires integration of Brillouin waveguides, E-O modulators, optical amplifiers, circulators, optical filters, and PDs. A number of hybrid and heterogeneously integrated platforms exist that combine many of these components. For example, butt-coupled TriPleX Si_3N_4 and InP chips [26] combine the advantages of low-loss Si_3N_4 waveguides with optical sources, amplifiers, modulators, and PDs offered by InP, and have formed the basis of fully-integrated MWP processing devices [32]. Initial studies have been undertaken to optimise the magnitude of Brillouin gain generated in Si_3N_4 waveguides [160], [161], however, the Brillouin gain coefficient in Si_3N_4 is orders of magnitude lower than As_2S_3 and SOI platforms. Although it is highly desirable to generate Brillouin gain in Si_3N_4 waveguides due to their widespread use and lack of non-linear losses, As_2S_3 and SOI platforms are currently more suitable for the SBS medium, as they have demonstrated much higher magnitudes of Brillouin gain.

SOI platforms leverage advances in CMOS fabrication methods, offering on-chip E-O modulators and PDs [34], [157]. Fully-integrated MWP processors have been achieved by pairing SOI chips with free-space coupled laser diodes [162]. Although these devices offer compact form factors, silicon lacks intrinsic second order optical nonlinearity, and is therefore doped to enable E-O modulation [163]. This introduces a trade-off between device bandwidth, losses, and modulation efficiency, especially at high RF frequencies [164].

Thin-film $LiNbO_3$ modulators are positioned to greatly improve the link performance of integrated MWP processors as they offer record-low $V_{\pi_{RF}}$ [164], [165], [166]. The integration of etched $LiNbO_3$ modulators with InP lasers [167] and micro transfer printed [168] amplifiers [169] offer an attractive path forward for integrated platforms used in high-performance MWP processors.

Care must be taken to minimise reflections of the Brillouin pump, which are caused by refractive index changes between materials. As discussed in Section IV, reflections must be minimised in systems that use backwards Brillouin processing to avoid degradation to the RF link performance [93]. The vertically tapered interface between Ge:SiO_2 and As_2S_3 that Lai et al. demonstrated [94] is an attractive method to achieve low-loss and low reflection interfaces in heterogeneously integrated MWP systems. Demonstrations of similar low-reflection transitions in future integrated Brillouin MWP processing platforms are essential to improve device performance.

Brillouin microwave processors require integration of circulators with isolation in the order of 30 dB to separate the Brillouin pump and probe. As discussed in Section IV, magneto-optical materials are difficult to implement in chip-scale devices, which leads to fabrication complexities [147]. Hence, acousto-optic non-reciprocal devices based on the same materials used in the MWP processor are an attractive alternative. Demonstrations of acousto-optic non-reciprocal devices using silicon [155], Si_3N_4 [149], and $LiNbO_3$ [170] waveguides highlight that non-reciprocal elements can be paired with many existing integrated MWP processing platforms. However, the efficiency and isolation exhibited by acousto-optic non-reciprocal devices must be improved to meet the requirements for Brillouin-based processors. For example, this can be achieved by increasing the efficiency of acoustic wave transducers [155], or reducing acoustic losses [170].

For MWP processors to be adopted in RF systems, their noise figure, linearity, and insertion loss must be competitive with their traditional RF electronic counterparts [17]. Generally, it is desirable to achieve low-loss transmission with noise figure below 10 dB and high linearity with SFDR exceeding 120 dB.$Hz^{2/3}$ [17], [79]. However, most integrated microwave photonic systems do not meet these metrics, or do not report them. Recent demonstrations of MWP filters with optimised link performance have come close to the target metrics, using a combination of fibre-based and chip-based components [45], [46], [158]. For example, Daulay et al. reported an MWP filter using on-chip processing that achieved a link gain of 10 dB, and noise figure of 15 dB, and SFDR of 116 dB.$Hz^{2/3}$ [158]. This performance was enabled using low-biasing, high power lasers and optical amplifiers [158]. When the same MWP filter was optimised to maximise linearity, an SFDR of 123 dB.$Hz^{2/3}$ was observed [158]. Although the noise figure and linearity were not all optimised simultaneously, this device recorded highest linearity, and lowest noise figure in an MWP link that uses on-chip processing to-date [158]. However, this level of performance is yet to be demonstrated in fully-integrated MWP processors. To bridge this performance gap, low loss waveguides [171], [172], [173], low $V_{\pi_{RF}}$ modulators [165], on-chip lasers with high power and low RIN noise [174], [175], low noise optical amplifiers [175], [176], and high-power PDs [168], [177], [178] must be integrated into a single platform.

To reduce the loss associated with converting between RF and optical domains multiple times, it is desirable to implement all the required functionalities in a single MWP link. Although many MWP processors have been used to demonstrate multiple RF processing functionalities [48], [158], [179], they only demonstrate a single RF processing function at any given time. This motivates future work to implement MWP processors that simultaneously achieve multiple RF processing functionalities in one optimised MWP link. Reza et al. performed a theoretical analysis of a fully-integrated MWP beamformer that combines frequency conversion and phase shift beamforming [44]. Through simulations they showed that the overall RF link gain of the multi-functional MWP device was comparable to single function MWP devices, essentially halving the link gain penalty by distributing it between two RF processing functionalities. This highlights the advantages of combining multiple RF processing functionalities into a single MWP link.

C. Size and Power Considerations

It is desirable to reduce the pump power required to generate SBS gain in Brillouin waveguides. Although RF interferometric processing techniques reduce the pump power required by Brillouin-based MWP processors [73], [93], [115], relatively large pump powers are still required to generate Brillouin gain over a wide bandwidth. For example, approximately 350 mW of coupled pump power was used by McKay et al. to generate 4 dB of Brillouin gain over a 400 MHz bandwidth [73] in a Ge:SiO_2-As_2S_3 PIC [94]. By analysing (13), the magnitude of Brillouin gain generated for a fixed pump power is related to the figure of merit (FOM), $G_{SBS}L_{eff}$, and determines how effective a material platform is at generating Brillouin gain [63]. Increases to both the Brillouin gain coefficient and the effective waveguide length are needed to reduce the required pump power. The former is improved by developing new Brillouin processing platforms and materials, such as fully-etched As_2S_3 waveguides [63], which have larger Brillouin gain coefficients than traditional As_2S_3 rib waveguides. The latter is increased by reducing waveguide losses of the Brillouin medium, which is currently dominated by sidewall scattering [180].

The form factor of each component must be considered to ensure the device is contained in the half-wavelength spacing between PAA elements, which is only 3 mm at 50 GHz. Many

components in the design presented in Fig. 19 are sufficiently compact and introduce no significant form factor limitations. These include MRRs, which have a bend radius of approximately 100 μm [171], [181], and PDs, which typically have maximum linear dimensions of only tens of microns [168], [177], [178]. Optical gain sections used for SOAs and laser sources are slightly longer with lengths close to 1 mm [168], [182]. While Brillouin As_2S_3 waveguides can require interaction lengths exceeding 6 cm [63], they have been incorporated in compact spirals with dimensions of less than 1 mm^2 [63], as discussed in Section IV. On-chip PPER waveguides typically require shorter interaction lengths, with a recent demonstration using Brillouin waveguides with only 17 mm length [110], which can easily be integrated into a footprint less than 1 mm^2.

Most work on high-performance modulators to-date has focused on lowering the $V_{\pi_{RF}}$, however, considerations must be made to ensure these devices maintain compact linear dimensions for deployment in space-constrained applications, such as PAAs. For example, the lowest $V_{\pi_{RF}}$ of an E-O modulator is 2.12 V at 50 GHz [165] and has a length of 2 cm, which can be challenging to integrate at each element of a PAA where space is highly constrained. However, folded [183], [184], [185], or spiral [186] E-O modulators have smaller maximum linear dimension when compared to their straight counterparts, and are attractive solutions for space constrained applications, such as at every element of a PAA. Similarly, acousto-optic non-reciprocal devices have been folded to reduce their on-chip footprint, as demonstrated by Kittlaus et al. [155].

VI. Conclusion

In conclusion, we reviewed recent advances to microwave photonic processors that use on-chip SBS to enable key RF processing functionalities for possible implementation in future PAAs, including filters, phase shifters, time delays, mixers, and frequency sources. The performance and functionality of these Brillouin-based devices has been enhanced by recent demonstrations of novel platforms that facilitate high-performance integrated Brillouin microwave processing. These integrated Brillouin platforms, along with recent advances in on-chip photonic components, stand to greatly reduce the form factor of microwave photonic processors when compared to current RF solutions with equivalent frequency operating range, bringing these devices closer towards real-world applications. We discussed challenges that must be overcome to implement fully-integrated SBS microwave processors for element-level beamforming in PAAs, whilst meeting demanding RF link performance requirements. In doing so, we have highlighted how on-chip SBS provides a path to enable compact microwave processors with wideband capability unmatched by traditional RF electronic solutions.

Acknowledgment

We acknowledge the ARC Grants DP190100992, DP200101893, and DP220101431 and fruitful on-going collaboration with our collaborators, Prof Michael Steel, Prof Christopher Poulton, Prof Steve Madden and Dr Bill Corcoran. We would like to thank Dr Stu Milner, Keith Kelly, Dr James Coyte, Nicholas Athanasios, and Ziqian Zhang for valuable feedback during the preparation of the manuscript. We would also like to thank Dr Yang Liu and Dr Alvaro Casas-Bedoya for their contributions to the design of the photonic chip shown in Figs. 1 and 6.

References

[1] *DARPA*, Compact front-end filters at the element-level (COFFEE), Jun. 2021. Accessed: Apr. 10, 2022. [Online]. Available: https://www.darpa.mil/news-events/2021-06-10

[2] G. Yang, Y. Zhang, and S. Zhang, "Wide-band and wide-angle scanning phased array antenna for mobile communication system," *IEEE Open J. Antennas Propag.*, vol. 2, no. Dec. 2020, pp. 203–212, 2021.

[3] L. Gao and G. M. Rebeiz, "A 22–44-GHz phased-array receive beamformer in 45-nm CMOS SOI for 5G applications with 3–3.6-dB NF," *IEEE Trans. Microw. Theory Tech.*, vol. 68, no. 11, pp. 4765–4774, Nov. 2020.

[4] C. Waldschmidt, J. Hasch, and W. Menzel, "Automotive radar – from first efforts to future systems," *IEEE J. Microw.*, vol. 1, no. 1, pp. 135–148, Jan. 2021.

[5] S. Pan, X. Ye, Y. Zhang, and F. Zhang, "Microwave photonic array radars," *IEEE J. Microw.*, vol. 1, no. 1, pp. 176–190, Jan. 2021.

[6] P. Hu, Q. Bao, and Z. Chen, "Target detection and localization using non-cooperative frequency agile phased array radar illuminator," *IEEE Access*, vol. 7, pp. 111277–111286, 2019.

[7] A. H. Naqvi and S. Lim, "Review of recent phased arrays for millimeter-wave wireless communication," *Sensors (Switzerland)*, vol. 18, no. 10, 2018, Art. no. 3194.

[8] S. H. Talisa, K. W. O'Haver, T. M. Comberiate, M. D. Sharp, and O. F. Somerlock, "Benefits of digital phased array radars," *Proc. IEEE*, vol. 104, no. 3, pp. 530–543, Mar. 2016.

[9] R. J. Mailloux, *Phased Array Antenna Handbook*. Norwood, MA, USA: Artech House, 2018.

[10] D. Parker and D. C. Zimmermann, "Phased arrays - part I: Theory and architectures," *IEEE Trans. Microw. Theory Tech.*, vol. 50, no. 3, pp. 678–687, Mar. 2002.

[11] P. J. Matthews, "Analog and digital photonics for future military systems," in *Proc. Opt. Fiber Commun. Conf.*, 2014, pp. 3–5.

[12] S. Mahon, "The 5G effect on RF filter technologies," *IEEE Trans. Semicond. Manuf.*, vol. 30, no. 4, pp. 494–499, Nov. 2017.

[13] Y. Yang, L. Gao, and S. Gong, "X-band miniature filters using lithium niobate acoustic resonators and bandwidth widening technique," *IEEE Trans. Microw. Theory Tech.*, vol. 69, no. 3, pp. 1602–1610, Mar. 2021.

[14] M. Torpey, A. Robson, and R. S. Howell, "Reconfigurable bandpass filter using SLCFET technology," in *Proc. IEEE MTT-S Int. Microw. Filter Work.*, 2021, pp. 262–264.

[15] S. Dai, S. A. Bhave, and R. Wang, "Octave-tunable magnetostatic wave YIG resonators on a chip," *IEEE Trans. Ultrason. Ferroelect. Freq. Control*, vol. 67, no. 11, pp. 2454–2460, Nov. 2020.

[16] J. D. Costa et al., "Compact tunable YIG-based RF resonators," *Appl. Phys. Lett.*, vol. 118, no. 16, 2021, Art. no. 162406.

[17] D. Marpaung, J. Yao, and J. Capmany, "Integrated microwave photonics," *Nat. Photon.*, vol. 13, no. 2, pp. 80–90, Feb. 2019.

[18] B. Barakat et al., "6 G opportunities arising from Internet of Things use cases: A review paper," *Future Internet*, vol. 13, no. 6, pp. 1–29, 2021.

[19] S. Pan and Y. Zhang, "Microwave photonic radars," *J. Lightw. Technol.*, vol. 38, pp. 1–1, 2020.

[20] Y. Liu, Z. Zhang, M. Burla, and B. J. Eggleton, "11-GHz-Bandwidth photonic radar using MHz electronics," *Laser Photon. Rev.*, vol. 16, 2022, Art. no. 2100549.

[21] V. J. Urick, J. D. Mckinney, and K. J. Williams, *Fundamental of Mircorwave Photonics*. Hoboken, NJ, USA: Wiley, Feb. 2015.

[22] J. M. Ramirez et al., "III-V-on-Silicon integration: From hybrid devices to heterogeneous photonic integrated circuits," *IEEE J. Sel. Top. Quantum Electron.*, vol. 26, no. 2, Mar./Apr. 2020, Art. no. 6100213.

[23] A. Boes, B. Corcoran, L. Chang, J. Bowers, and A. Mitchell, "Status and potential of lithium niobate on insulator (LNOI) for photonic integrated circuits," *Laser Photon. Rev.*, vol. 12, no. 4, pp. 1–19, 2018.

[24] T. Komljenovic, "Photonic integrated circuits using heterogeneous integration on silicon," *Proc. IEEE*, vol. 106, no. 12, pp. 2246–2257, Dec. 2018.

[25] N. Margalit et al., "Perspective on the future of silicon photonics and electronics," *Appl. Phys. Lett.*, vol. 118, no. 22, 2021, Art. no. 220501.

[26] A. Leinse et al., "Hybrid Interconnection of InP and TriPleX Photonic Integrated Circuits for New Module Functionality," in *Optical Interconnects XIX*, H. Schröder and R. T. Chen, Eds., Bellingham, WA, USA: SPIE, Apr. 2019, pp. 1–10.

[27] L. Chang, S. Liu, and J. E. Bowers, "Integrated optical frequency comb technologies," *Nat. Photon.*, vol. 16, no. 2, pp. 95–108, 2022.

[28] J. Hu et al., "Reconfigurable radiofrequency filters based on versatile soliton microcombs," *Nat. Commun.*, vol. 11, no. 1, pp. 1–9, 2020.

[29] Y. Liu, A. Choudhary, D. Marpaung, and B. J. Eggleton, "Integrated microwave photonic filters," *Adv. Opt. Photon.*, vol. 12, no. 2, pp. 485–555, 2020.

[30] M. Burla et al., "On-chip programmable ultra-wideband microwave photonic phase shifter and true time delay unit," *Opt. Lett.*, vol. 39, no. 21, pp. 6181–6184, 2014.

[31] S. Pan and Y. Zhang, "Tunable and wideband microwave photonic phase shifter based on a single-sideband polarization modulator and a polarizer," *Opt. Lett.*, vol. 37, no. 21, pp. 4483–4485, 2012.

[32] C. Tsokos et al., "True time delay optical beamforming network based on hybrid InP-Silicon nitride integration," *J. Lightw. Technol.*, vol. 39, no. 18, pp. 5845–5854, 2021.

[33] P. Zheng et al., "A seven bit silicon optical true time delay line for ka-band phased array antenna," *IEEE Photon. J.*, vol. 11, no. 4, Aug. 2019, Art. no. 5501809.

[34] C. Zhu et al., "Silicon integrated microwave photonic beamformer," *Optica*, vol. 7, no. 9, pp. 1162–1170, 2020.

[35] C. G. Bottenfield and S. E. Ralph, "High-performance fully integrated silicon photonic microwave mixer subsystems," *J. Lightw. Technol.*, vol. 38, no. 19, pp. 5536–5545, 2020.

[36] C. G. Bottenfield, V. A. Thomas, G. Saha, R. DeSalvo, and S. E. Ralph, "A silicon microwave photonic down-converter," *IET Conf. Publ.*, vol. 2019, no. CP765, pp. 1–4, 2019.

[37] G. K. Hasanuzzaman, S. Iezekiel, and A. Kanno, "W-band optoelectronic oscillator," *IEEE Photon. Technol. Lett.*, vol. 32, no. 13, pp. 771–774, Jul. 2020.

[38] E. A. Kittlaus et al., "A low-noise photonic heterodyne synthesizer and its application to millimeter-wave radar," *Nat. Commun.*, vol. 12, no. 1, Dec. 2021, Art. no. 4397.

[39] E. Lucas et al., "Ultralow-noise photonic microwave synthesis using a soliton microcomb-based transfer oscillator," *Nat. Commun.*, vol. 11, no. 1, pp. 1–8, 2020.

[40] J. Liu et al., "Photonic microwave generation in the X- and K-band using integrated soliton microcombs," *Nat. Photon.*, vol. 14, no. 8, pp. 486–491, 2020.

[41] C. Roeloffzen, P. van Dijk, D. Marpaung, M. Burla, and L. Zhuang, "Development of a broadband integrated optical beamformer for ku-band phased array antennas," in *Proc. 34th ESA Antenna Work.*, 2012, pp. 3–5.

[42] M. Burla et al., "Integrated photonic Ku-band beamformer chip with continuous amplitude and delay control," *IEEE Photon. Technol. Lett.*, vol. 25, no. 12, pp. 1145–1148, Jun. 2013.

[43] V. C. Duarte et al., "Modular coherent photonic-aided payload receiver for communications satellites," *Nature Commun.*, vol. 10, pp. 1–9, 2019.

[44] M. Reza et al., "Design and performance estimation of a photonic integrated beamforming receiver for scan-on-receive synthetic aperture radar," *J. Lightw. Technol.*, vol. 39, no. 24, pp. 7588–7599, 2021.

[45] Y. Liu, J. Hotten, A. Choudhary, B. J. Eggleton, and D. Marpaung, "All-optimized integrated RF photonic notch filter," *Opt. Lett.*, vol. 42, no. 22, pp. 4631–4634, Nov. 2017.

[46] G. Liu et al., "Integrated microwave photonic spectral shaping for linearization and spurious-free dynamic range enhancement," *J. Lightw. Technol.*, vol. 39, no. 24, pp. 7551–7562, Dec. 2021.

[47] L. Zhuang, C. G. H. Roeloffzen, M. Hoekman, K.-J. Boller, and A. J. Lowery, "Programmable photonic signal processor chip for radiofrequency applications," *Optica*, vol. 2, no. 10, pp. 854–859, Oct. 2015.

[48] D. Pérez et al., "Multipurpose silicon photonics signal processor core," *Nat. Commun.*, vol. 8, no. 1, Dec. 2017, Art. no. 636.

[49] J. Capmany, J. Mora, D. Pastor, and B. Ortega, "High-quality online-reconfigurable microwave photonic transversal filter with positive and negative coefficients," *IEEE Photon. Technol. Lett.*, vol. 17, no. 12, pp. 2730–2732, Dec. 2005.

[50] Y. Xie et al., "System-level performance of chip-based brillouin microwave photonic bandpass filters," *J. Lightw. Technol.*, vol. 37, no. 20, pp. 5246–5258, 2019.

[51] I. Visscher et al., "Broadband true time delay microwave photonic beamformer for phased array antennas," in *Proc. 13th Eur. Conf. Antennas Propag.*, 2019, pp. 1–5.

[52] J. Wang et al., "Subwavelength grating enabled on-chip ultra-compact optical true time delay line," *Sci. Rep.*, vol. 6, no. 1, pp. 1–10, 2016.

[53] G. Wang et al., "Continuously tunable true-time delay lines based on a one-dimensional grating waveguide for beam steering in phased array antennas," *Appl. Opt.*, vol. 57, pp. 4998–5003, 2018.

[54] B. J. Eggleton, C. G. Poulton, P. T. Rakich, M. J. Steel, and G. Bahl, "Brillouin integrated photonics," *Nat. Photon.*, vol. 13, no. 10, pp. 664–677, 2019.

[55] B. Vidal, M. A. Piqueras, and J. Martí, "Tunable and reconfigurable photonic microwave filter based on stimulated brillouin scattering," *Opt. Lett.*, vol. 32, no. 1, pp. 23–25, 2007.

[56] W. Zhang and R. A. Minasian, "Widely tunable single-passband microwave photonic filter based on stimulated Brillouin scattering," *IEEE Photon. Technol. Lett.*, vol. 23, no. 23, pp. 1775–1777, Dec. 2011.

[57] S. Preussler, A. Zadok, A. Wiatrek, M. Tur, and T. Schneider, "Enhancement of spectral resolution and optical rejection ratio of Brillouin optical spectral analysis using polarization pulling," *Opt. Exp.*, vol. 20, no. 13, pp. 14734–14745, Jun. 2012 .

[58] T. Schneider, D. Hannover, and M. Junker, "Theoretical and experimental investigation of brillouin scattering in optical fibers for the generation of millimeter waves," *J. Lightw. Technol.*, vol. 24, no. 1, pp. 295–304, Jan. 2006.

[59] M. González Herráez, K. Y. Song, and L. Thévenaz, "Arbitrary-bandwidth Brillouin slow light in optical fibers," *Opt. Exp.*, vol. 14, no. 4, pp. 1395–1400, 2006.

[60] A. Byrnes et al., "Photonic chip based tunable and reconfigurable narrowband microwave photonic filter using stimulated brillouin scattering," *Opt. Exp.*, vol. 20, no. 17, pp. 18836–18845, 2012.

[61] A. Choudhary et al., "Tailoring of the brillouin gain for on-chip widely tunable and reconfigurable broadband microwave photonic filters," *Opt. Lett.*, vol. 41, no. 3, pp. 436–439, 2016.

[62] R. Pant et al., "On-chip stimulated Brillouin scattering," *Opt. Exp.*, vol. 19, no. 9, pp. 8285–8290, Apr. 2011 .

[63] B. Morrison et al., "Compact Brillouin devices through hybrid integration on silicon," *Optica*, vol. 4, no. 8, pp. 847–854, 2017.

[64] R. Van Laer, B. Kuyken, D. Van Thourhout, and R. Baets, "Interaction between light and highly confined hypersound in a silicon photonic nanowire," *Nat. Photon.*, vol. 9, no. 3, pp. 199–203, Mar. 2015.

[65] H. Shin et al., "Tailorable stimulated Brillouin scattering in nanoscale silicon waveguides," *Nat. Commun.*, vol. 4, pp. 1–10, 2013.

[66] H. Shin et al., "Control of coherent information via on-chip photonic-phononic emitter-receivers," *Nat. Commun.*, vol. 6, pp. 2–9, 2015.

[67] S. Gundavarapu et al., "Sub-hertz fundamental linewidth photonic integrated Brillouin laser," *Nat. Photon.*, vol. 13, no. 1, pp. 60–67, Jan. 2019.

[68] H. Lee et al., "Chemically etched ultrahigh-q wedge-resonator on a silicon chip," *Nat. Photon.*, vol. 6, no. 6, pp. 369–373, 2012.

[69] M. Garrett et al., "Low-RF-loss and large-rejection reconfigurable Brillouin-based RF photonic bandpass filter," *Opt. Lett.*, vol. 45, no. 13, pp. 3705–3708, 2020.

[70] J. Li, H. Lee, and K. J. Vahala, "Microwave synthesizer using an on-chip Brillouin oscillator," *Nat. Commun.*, vol. 4, no. 1, Oct. 2013, Art. no. 2097.

[71] M. Merklein et al., "Widely tunable, low phase noise microwave source based on a photonic chip," *Opt. Lett.*, vol. 41, no. 20, pp. 4633–4636, 2016.

[72] Z. Zhu, D.-Y. Choi, S. J. Madden, B. J. Eggleton, and M. Merklein, "High-conversion-gain and deep-image-rejection Brillouin chip-based photonic RF mixer," *Opt. Lett.*, vol. 45, no. 19, pp. 5571–5574, 2020.

[73] L. McKay et al., "Chip-based broadband microwave photonic mixer with image rejection," in *Proc. Int. Top. Meeting Microw. Photon.*, Nov. 2021, pp. 1–4.

[74] M. Pagani et al., "Tunable wideband microwave photonic phase shifter using on-chip stimulated Brillouin scattering," *Opt. Exp.*, vol. 22, no. 23, pp. 28810–28818, Nov. 2014.

[75] L. McKay et al., "Broadband Brillouin-based phase shifter with phase amplification in a silicon waveguide," *Optica*, vol. 6, no. 7, 2019, Paper SM4O.4.

[76] L. McKay et al., "Broadband Brillouin phase shifter utilizing RF interference: Experimental demonstration and theoretical analysis," *J. Lightw. Technol.*, vol. 38, no. 14, pp. 3624–3636, 2020.

[77] I. Aryanfar et al., "Chip-based Brillouin radio frequency photonic phase shifter and wideband time delay," *Opt. Lett.*, vol. 42, no. 7, pp. 1313–1316, 2017.

[78] L. McKay et al., "Integrated microwave photonic true-time delay with interferometric delay enhancement based on Brillouin scattering and microring resonators," *Opt. Exp.*, vol. 28, no. 24, pp. 36020–36032, Nov. 2020.

[79] J. D. McKinney et al., "Sub-10-dB noise figure in a multiple-GHz analog optical link," *IEEE Photon. Technol. Lett.*, vol. 19, no. 7, pp. 465–467, Apr. 2007.

[80] T. W. Jeffrey, *Phased-Array Radar Design: Application of Radar Fundamentals*. London, U.K.: Inst. Eng. Technol., Jan. 2009.

[81] W. Ng et al., "The first demonstration of an optically steered microwave phased array antenna using true-time-delay," *J. Lightw. Technol.*, vol. 9, no. 9, pp. 1124–1131, 1991.

[82] W. Liu and S. Weiss, *Wideband Beamforming*. Chichester, U.K.:Wiley, Mar. 2010.

[83] D. Marpaung, "High dynamic range analog photonic links : Design and implementation," Ph.D. dissertation, Univ. Twente, Enschede, The Netherlands, Aug. 2009.

[84] Z. Zhu et al., "Positive link gain microwave photonic bandpass filter using Si_3N_4-ring-enabled sideband filtering and carrier suppression," *Opt. Exp.*, vol. 27, no. 22, pp. 31727–31740, 2019.

[85] X. Han, E. Xu, and J. Yao, "Tunable single bandpass microwave photonic filter with an improved dynamic range," *IEEE Photon. Technol. Lett.*, vol. 28, no. 1, pp. 11–14, Jan. 2016.

[86] O. Daulay, G. Liu, and D. Marpaung, "Microwave photonic notch filter with integrated phase-to-intensity modulation transformation and optical carrier suppression," *Opt. Lett.*, vol. 46, no. 3, pp. 488–491, 2021.

[87] G. Liu, O. Daulay, Q. Tan, H. Yu, and D. Marpaung, "Linearized phase modulated microwave photonic link based on integrated ring resonators," *Opt. Exp.*, vol. 28, pp. 38603–38615, 2020.

[88] W. Zhu et al., "Dynamic range improvement of a microwave photonic link based on Brillouin processing," *IEEE Photon. Technol. Lett.*, vol. 28, no. 23, pp. 2681–2684, Dec. 2016.

[89] Y. Liu, D. Marpaung, A. Choudhary, J. Hotten, and B. J. Eggleton, "Link performance optimization of chip-based Si3N4 microwave photonic filters," *J. Lightw. Technol.*, vol. 36, no. 19, pp. 4361–4370, 2018.

[90] Y. Liu, A. Choudhary, D. Marpaung, and B. J. Eggleton, "Chip-based Brillouin processing for phase control of RF signals," *IEEE J. Quantum Electron.*, vol. 54, no. 3, Jun. 2018, Art. no. 6300413.

[91] E. Sánchez, D. Pérez-López, P. DasMahapatra, and J. Capmany, "Modeling amplified arbitrary filtered microwave photonic links and systems," *Opt. Exp.*, vol. 29, no. 10, pp. 14757–14772, May 2021.

[92] S. J. Madden et al., "Long, low loss etched As_2S_3 chalcogenide waveguides for all-optical signal regeneration," *Opt. Exp.*, vol. 15, no. 22, pp. 14414–14421, 2007.

[93] M. Garrett et al., "Multi-band and frequency-agile chip-based rf photonic filter for ultra-deep interference rejection," *J. Lightw. Technol.*, vol. 40, pp. 1672–1680, 2022.

[94] C. K. Lai et al., "Hybrid chalcogenide-germanosilicate waveguides for high performance stimulated brillouin scattering applications," *Adv. Funct. Mater.*, vol. 32, no. 3, pp. 1–8, 2021.

[95] N. T. Otterstrom, R. O. Behunin, E. A. Kittlaus, Z. Wang, and P. T. Rakich, "A silicon Brillouin laser," *Science (80-.).*, vol. 360, no. 6393, pp. 1113–1116, Jun. 2018.

[96] L. Brillouin, "Diffusion de la lumière et des rayons x par un corps transparent homogène," *Ann. Phys.*, vol. 9, pp. 88–122, 1922.

[97] R. W. Boyd, "Stimulated brillouin and stimulated Rayleigh scattering," in *Nonlinear Optics*. Amsterdam, The Netherlands: Elsevier, 2003, pp. 409–450.

[98] G. P. Agrawal, *Nonlinear Fiber Optics*, 5th ed. Cambridge, MA, USA: Academic, 2013.

[99] B. J. Eggleton, C. G. Poulton, and R. Pant, "Inducing and harnessing stimulated Brillouin scattering in photonic integrated circuits," *Adv. Opt. Photon.*, vol. 5, no. 4, pp. 536–587, Dec. 2013.

[100] C. Wolff, M. J. A. Smith, B. Stiller, and C. G. Poulton, "Brillouin scattering–theory and experiment: Tutorial," *J. Opt. Soc. Amer. B*, vol. 38, no. 4, pp. 1243–1269, Apr. 2021.

[101] M. Pagani, D. Marpaung, and B. J. Eggleton, "Ultra-wideband microwave photonic phase shifter with configurable amplitude response," *Opt. Lett.*, vol. 39, pp. 5854–5857, 2014.

[102] M. Merklein, B. Stiller, and B. J. Eggleton, "Brillouin-based light storage and delay techniques," *J. Opt.*, vol. 20, no. 8, Aug. 2018, Art. no. 083003.

[103] A. Choudhary et al., "Advanced integrated microwave signal processing with giant on-chip Brillouin gain," *J. Lightw. Technol.*, vol. 35, no. 4, pp. 846–854, 2017.

[104] J. Song et al., "Stimulated brillouin scattering in low-loss $Ge_{25}Sb_{10}S_{65}$ chalcogenide waveguides," *J. Lightw. Technol.*, vol. 39, no. 15, pp. 5048–5053, 2021.

[105] E. A. Kittlaus, H. Shin, and P. T. Rakich, "Large brillouin amplification in silicon," *Nat. Photon.*, vol. 10, no. 7, pp. 463–467, 2016.

[106] N. T. Otterstrom et al., "Resonantly enhanced nonreciprocal silicon Brillouin amplifier," *Optica*, vol. 6, no. 9, pp. 1117–1123, Sep. 2019.

[107] M. Merklein et al., "Stimulated Brillouin scattering in photonic integrated circuits: Novel applications and devices," *IEEE J. Sel. Top. Quantum Electron.*, vol. 22, no. 2, pp. 336–346, Mar./Apr. 2016.

[108] J. Song et al., "On-chip stimulated Brillouin scattering in As2S3 waveguides with soft claddings of benzocyclobutene," *Opt. Commun.*, vol. 509, no. Nov. 2021, 2022, Art. no. 127879.

[109] P. T. Rakich, C. Reinke, R. Camacho, P. Davids, and Z. Wang, "Giant enhancement of stimulated Brillouin scattering in the subwavelength limit," *Phys. Rev. X*, vol. 2, 2012, Art. no. 011008.

[110] S. Gertler et al., "Narrowband microwave-photonic notch filters using Brillouin-based signal transduction in silicon," *Nat. Commun.*, vol. 13, no. 1, Dec. 2022, Art. no. 1947.

[111] A. Choudhary, Y. Liu, D. Marpaung, and B. J. Eggleton, "On-chip Brillouin filtering of RF and optical signals," *IEEE J. Sel. Top. Quantum Electron.*, vol. 24, no. 6, Nov./Dec. 2018, Art. no. 7600211.

[112] A. Loayssa, R. Hernández, D. Benito, and S. Galech, "Characterization of stimulated Brillouin scattering spectra by use of optical single-sideband modulation," *Opt. Lett.*, vol. 29, pp. 638–640, 2004.

[113] B. Morrison et al., "Tunable microwave photonic notch filter using on-chip stimulated Brillouin scattering," *Opt. Commun.*, vol. 313, pp. 85–89, 2014.

[114] R. Parihar, R. Dhawan, S. Goel, B. O. Subham, and A. Choudhary, "Design of microwave photonic subsystems using Brillouin scattering," *J. Lightw. Technol.*, vol. 39, no. 4, pp. 977–991, Feb. 2021.

[115] D. Marpaung et al., "Low-power, chip-based stimulated Brillouin scattering microwave photonic filter with ultrahigh selectivity," *Optica*, vol. 2, no. 2, pp. 76–83, 2015.

[116] A. Casas-Bedoya, B. Morrison, M. Pagani, D. Marpaung, and B. J. Eggleton, "Tunable narrowband microwave photonic filter created by stimulated Brillouin scattering from a silicon nanowire," *Opt. Lett.*, vol. 40, no. 17, pp. 4154–4157, Sep. 2015.

[117] Y. Liu et al., "Integration of brillouin and passive circuits for enhanced radio-frequency photonic filtering," *APL Photon.*, vol. 4, no. 10, Oct. 2019, Art. no. 106103.

[118] Y. Liu, D. Marpaung, A. Choudhary, and B. J. Eggleton, "Lossless and high-resolution RF photonic notch filter," *Opt. Lett.*, vol. 41, no. 22, pp. 5306–5309, Nov. 2016.

[119] E. A. Kittlaus, P. Kharel, N. T. Otterstrom, Z. Wang, and P. T. Rakich, "RF-Photonic filters via on-chip photonic-phononic emit-receive operations," *J. Lightw. Technol.*, vol. 36, no. 13, pp. 2803–2809, 2018.

[120] S. Gertler, E. A. Kittlaus, N. T. Otterstrom, and P. T. Rakich, "Tunable microwave-photonic filtering with high out-of-band rejection in silicon," *APL Photon.*, vol. 5, no. 9, pp. 1–30, 2020.

[121] S. Gertler, E. A. Kittlaus, N. T. Otterstrom, P. Kharel, and P. T. Rakich, "Microwave filtering using forward Brillouin scattering in photonic-phononic emit-receive devices," *J. Lightw. Technol.*, vol. 38, no. 19, pp. 5248–5261, Oct. 2020.

[122] S. Gertler et al., "Narrowband microwave-photonic notch filtering using Brillouin interactions in silicon," in *Proc. Conf. Lasers Electro- Opt.*, Washington, DC, USA: OSA, 2021, Paper S W3A.4.

[123] M. B. Ayun, A. Schwarzbaum, S. Rosenberg, M. Pinchas, and S. Sternklar, "Photonic radio frequency phase-shift amplification by radio frequency interferometry," *Opt. Lett.*, vol. 40, no. 21, pp. 4863–4866, 2015.

[124] S. Jang, R. Lu, J. Jeong, and M. P. Flynn, "A 1-GHz 16-Element four-beam true-time-delay digital beamformer," *IEEE J. Solid-State Circuits*, vol. 54, no. 5, pp. 1304–1314, May 2019.

[125] G. Lenz, B. J. Eggleton, C. K. Madsen, and R. E. Slusher, "Optical delay lines based on optical filters," *IEEE J. Quantum Electron.*, vol. 37, no. 4, pp. 525–532, Apr. 2001.

[126] P. A. Morton and J. B. Khurgin, "Microwave photonic delay line with separate tuning of the optical carrier," *IEEE Photon. Technol. Lett.*, vol. 21, no. 22, pp. 1686–1688, Nov. 2009.

[127] R. Pant et al., "Photonic-chip-based tunable slow and fast light via stimulated Brillouin scattering," *Opt. Lett.*, vol. 37, no. 5, pp. 969–971, Mar. 2012.

[128] Y. Okawachi et al., "Tunable all-optical delays via Brillouin slow light in an optical fiber," *Phys. Rev. Lett.*, vol. 94, pp. 1–4, 2005.

[129] K. Y. Song, M. G. Herráez, and L. Thévenaz, "Observation of pulse delaying and advancement in optical fibers using stimulated Brillouin scattering," *Opt. Exp.*, vol. 13, pp. 82-88, 2005.

[130] M. Merklein, B. Stiller, K. Vu, S. J. Madden, and B. J. Eggleton, "A chip-integrated coherent photonic-phononic memory," *Nature Commun.*, vol. 8, no. 1, pp. 1–7, 2017.

[131] S. Preussler, A. Wiatrek, K. Jamshidi, and T. Schneider, "Quasi-light-storage enhancement by reducing the Brillouin gain bandwidth," *Appl. Opt.*, vol. 50, pp. 4252–4256, 2011.

[132] K. Y. Song, K. Lee, and S. B. Lee, "Tunable optical delays based on Brillouin dynamic grating in optical fibers," *Opt. Exp.*, vol. 17, pp. 10344–10349, 2009.

[133] S. Chin and L. Thévenaz, "Tunable photonic delay lines in optical fibers," *Laser Photon. Rev.*, vol. 6, pp. 724–738, 2012.

[134] Y. Antman et al., "Experimental demonstration of localized Brillouin gratings with low off-peak reflectivity established by perfect golomb codes," *Opt. Lett.*, vol. 38, pp. 4701–4704, 2013.

[135] M. Merklein et al., "On-chip broadband nonreciprocal light storage," *Nanophotonics*, vol. 10, pp. 75–82, Jan. 2021.

[136] N. Choksi, Y. Liu, R. Ghasemi, and L. Qian, "Sub-megahertz spectral dip in a resonator-free twisted gain medium," *Nature Photon.*, vol. 16, pp. 1–7, Jul. 2022.

[137] S. S. A., A. B. Yelikar, and R. Pant, "Analogue of electromagnetically induced absorption in the microwave domain using stimulated Brillouin scattering," *Commun. Phys.*, vol. 3, no. 1, pp. 1–11, 2020.

[138] N. J. Athanasios et al., "On-chip all-optical polarisation pulling via stimulated brillouin scattering," in *Proc. Conf. Lasers Electro- Opt. Pacific Rim, CLEO-PR 2020 - Proc.*, 2020, pp. 9–11.

[139] D. Zhu and S. Pan, "Photonics-based microwave image-reject mixer," *Photonics*, vol. 5, no. 2, 2018, Art. no. 6.

[140] S. Wu and Y. Bar-Ness, "OFDM systems in the presence of phase noise: Consequences and solutions," *IEEE Trans. Commun.*, vol. 52, no. 11, pp. 1988–1996, Nov. 2004.

[141] K. Siddiq, M. K. Hobden, S. R. Pennock, and R. J. Watson, "Phase noise in FMCW radar systems," *IEEE Trans. Aerosp. Electron. Syst.*, vol. 55, no. 1, pp. 70–81, Feb. 2019.

[142] G. Serafino et al., "Toward a new generation of radar systems based on microwave photonic technologies," *J. Lightw. Technol.*, vol. 37, no. 2, pp. 643–650, 2019.

[143] J. Li, X. Yi, H. Lee, S. A. Diddams, and K. J. Vahala, "Electro-optical frequency division and stable microwave synthesis," *Science (80-.)*, vol. 345, no. 6194, pp. 309–313, Jul. 2014.

[144] L. Maleki, "The optoelectronic oscillator," *Nat. Photon.*, vol. 5, no. 12, pp. 728–730, Dec. 2011.

[145] Y. Zhang et al., "Monolithic integration of broadband optical isolators for polarization-diverse silicon photonics," *Optica*, vol. 6, no. 4, pp. 473–478, Apr. 2019.

[146] L. J. Aplet and J. W. Carson, "A faraday effect optical isolator," *Appl. Opt.*, vol. 3, no. 4, pp. 544–545, 1964.

[147] K. Srinivasan and B. J. H. Stadler, "Review of integrated magneto-optical isolators with rare-earth iron garnets for polarization diverse and magnet-free isolation in silicon photonics [Invited]," *Opt. Mater. Exp.*, vol. 12, no. 2, pp. 697–716, 2022.

[148] W. Yan et al., "Waveguide-integrated high-performance magneto-optical isolators and circulators on silicon nitride platforms," *Optica*, vol. 7, no. 11, pp. 1555–1562, 2020.

[149] H. Tian et al., "Magnetic-free silicon nitride integrated optical isolator," *Nat. Photon.*, vol. 15, no. 11, pp. 828–836, 2021.

[150] X. Huang and S. Fan, "Complete all-optical silica fiber isolator via stimulated Brillouin scattering," *J. Lightw. Technol.*, vol. 29, no. 15, pp. 2267–2275, 2011.

[151] C. G. Poulton et al., "Design for broadband on-chip isolator using stimulated Brillouin scattering in dispersion-engineered chalcogenide waveguides," *Opt. Exp.*, vol. 20, no. 19, 2012, Art. no. 21235.

[152] D. B. Sohn, S. Kim, and G. Bahl, "Time-reversal symmetry breaking with acoustic pumping of nanophotonic circuits," *Nat. Photon.*, vol. 12, no. 2, pp. 91–97, 2018.

[153] E. A. Kittlaus, N. T. Otterstrom, P. Kharel, S. Gertler, and P. T. Rakich, "Non-reciprocal interband Brillouin modulation," *Nat. Photon.*, vol. 12, no. 10, pp. 613–619, 2018.

[154] L. Huan, L. Qiyu, and M. Li, "Electromechanical Brillouin scattering in integrated planar photonics," *APL Photon.*, vol. 4, Aug. 2019, Art. no. 080802.

[155] E. A. Kittlaus et al., "Electrically driven acousto-optics and broadband non-reciprocity in silicon photonics," *Nature Photon.*, vol. 15, pp. 43–52, 2021.

[156] Y. Liu et al., "Circulator-free Brillouin photonic planar circuit," *Laser Photon. Rev.*, vol. 200048 1, pp. 1–7, 2021.

[157] X. Guo et al., "Versatile silicon microwave photonic spectral shaper," *APL Photon.*, vol. 6, no. 3, Mar. 2021, Art. no. 036106.

[158] O. Daulay et al., "Ultrahigh dynamic range and low noise figure programmable integrated microwave photonic filter," 2022, *arXiv:2203.04724*.

[159] P. Kaur et al., "Hybrid and heterogeneous photonic integration," *APL Photon.*, vol. 6, Jun. 2021, Art. no. 061102.

[160] R. Botter et al., "Guided-acoustic stimulated Brillouin scattering in silicon nitride photonic circuits," 2021, *arXiv:2112.00829*.

[161] F. Gyger et al., "Observation of stimulated Brillouin scattering in silicon nitride integrated waveguides," *Phys. Rev. Lett.*, vol. 124, no. 1, pp. 1–7, 2020.

[162] Y. Tao et al., "Hybrid-integrated high-performance microwave photonic filter with switchable response," *Photon. Res.*, vol. 9, pp. 1569–1580, 2021.

[163] A. Rahim et al., "Taking silicon photonics modulators to a higher performance level: State-of-the-art and a review of new technologies," *Adv. Photon.*, vol. 3, no. 2, pp. 1–23, 2021.

[164] M. Zhang, C. Wang, P. Kharel, D. Zhu, and M. Lončar, "Integrated lithium niobate electro-optic modulators: When performance meets scalability," *Optica*, vol. 8, no. 5, pp. 652–667, 2021.

[165] P. Kharel, C. Reimer, K. Luke, L. He, and M. Zhang, "Breaking voltage-bandwidth limits in integrated lithium niobate modulators using micro-structured electrodes: Erratum," *Optica*, vol. 8, no. 9, pp. 1218–1218, 2021.

[166] C. Wang et al., "Integrated lithium niobate electro-optic modulators operating at cmos-compatible voltages," *Nature*, vol. 562, pp. 101–104, 2018.

[167] A. Shams-Ansari et al., "Electrically-pumped high-power laser transmitter integrated on thin-film lithium niobate," *Optica*, vol. 9, no. 4, pp. 408–411, Apr. 2022.

[168] J. Zhang et al., "III-V-on-Si photonic integrated circuits realized using micro-transfer-printing," *APL Photon.*, vol. 4, no. 11, 2019, Art. no. 110803.

[169] C. Op de Beeck et al., "III/V-on-lithium niobate amplifiers and lasers," *Optica*, vol. 8, no. 10, pp. 1288–1289, Oct. 2021.

[170] C. J. Sarabalis et al., "Acousto-optic modulation of a wavelength-scale waveguide," *Optica*, vol. 8, pp. 477–483, 2021.

[171] C. G. H. Roeloffzen et al., "Low-loss Si3N4 TriPleX optical waveguides: Technology and applications overview," *IEEE J. Sel. Top. Quantum Electron.*, vol. 24, no. 4, pp. 1–21, Jul. 2018.

[172] K. Luke et al., "Wafer-scale low-loss lithium niobate photonic integrated circuits," *Opt. Exp.*, vol. 28, no. 8, pp. 24452–24458, 2020.

[173] M. A. Tran et al., "Ultra-low-loss silicon waveguides for heterogeneously integrated silicon/iii-v photonics," *Appl. Sci. (Switzerland)*, vol. 8, no. 7, 2018, Art. no. 1139.

[174] J. P. Epping et al., "Hybrid integrated silicon nitride lasers," in *Physics and Simulation of Optoelectronic Devices XXVIII*, M. Osiński, Y. Arakawa, and B. Witzigmann, Eds., Bellingham, WA, USA: SPIE, Mar. 2020, pp. 1–10.

[175] K. A. McKinzie et al., "InP high power monolithically integrated widely tunable laser and SOA array for hybrid integration," *Opt. Exp.*, vol. 29, no. 3, pp. 3490–3502, 2021.

[176] K. Van Gasse, R. Wang, and G. Roelkens, " 27 dB gain III–V-on-silicon semiconductor optical amplifier with $>$ 17 dBm output power," *Opt. Exp.*, vol. 27, no. 1, pp. 293–302, Jan. 2019.

[177] E. Rouvalis et al., "High-power and high-linearity photodetector modules for microwave photonic applications," *J. Lightw. Technol.*, vol. 32, pp. 3810–3816, 2014.

[178] K. Sun and A. Beling, "High-speed photodetectors for microwave photonics," *Appl. Sci. (Switzerland)*, vol. 9, 2019, Art. no. 623.

[179] X. Zou et al., "A multifunctional photonic integrated circuit for diverse microwave signal generation, transmission, and processing," *Laser Photon. Rev.*, vol. 13, pp. 1–10, 2019.

[180] C. G. Poulton et al., "Radiation modes and roughness loss in high index-contrast waveguides," *IEEE J. Sel. Topics Quantum Electron.*, vol. 12, no. 6, pp. 1306–1321, Nov. 2006.

[181] W. Bogaerts et al., "Silicon microring resonators," *Laser Photon. Rev.*, vol. 6, pp. 47–73, 2012.

[182] C. Op de Beeck et al., "Heterogeneous III-V on silicon nitride amplifiers and lasers via microtransfer printing," *Optica*, vol. 7, no. 5, pp. 386–393, 2020.
[183] S. Sun et al., "Folded heterogeneous silicon and lithium niobate mach–zehnder modulators with low drive voltage," *Micromachines*, vol. 12, no. 7, Jul. 2021, Art. no. 823.
[184] S. Nelan et al., "Compact W-band thin film lithium niobate foldedintensity modulator using a waveguide crossing," *Opt. Exp.*, vol. 30, no. 6, pp. 9193–9207, Mar. 2022.
[185] R. Walker et al., "50GHz gallium arsenide electro-optic modulators for spaceborne telecommunications," in *Proc. Int. Conf. SpOpt. – ICSO 2018*, N. Karafolas, Z. Sodnik, and B. Cugny, Eds., vol. 11180, Oct. 2018, Jul. 2019, pp. 1–9.
[186] A. E. Hassanien, A. O. Ghoname, E. Chow, L. L. Goddard, and S. Gong, "Compact MZI modulators on thin film Z-cut lithium niobate," *Opt. Exp.*, vol. 30, no. 3, pp. 4543–4552, 2022.

Matthew Garrett (Student Member, IEEE) received the B.E. degree in electrical engineering (Hons.) from the University of New South Wales, Sydney, NSW, Australia, in 2016. He is currently working toward the Ph.D. degree in integrated microwave photonic signal processing with The University of Sydney, Sydney. From 2016 to 2019, he designed, tested and installed electronics for radio frequency and low-power sensing applications. His research interests include nonlinear optics, integrated microwave photonics and their applications in commercial and defence systems.

Moritz Merklein received the Ph.D. degree from the University of Sydney, Sydney, NSW, Australia, in 2018. He is currently a Research Fellow with the University of Sydney and a Team Leader within the Jericho Smart Sensing Lab (JSSL). His research was recognised with several awards, including the Rita and John Cornforth Graduate Medal 2019, Royal Society of NSW Jak Kelly Award 2017, and Australian Institute of Physics NSW Medal for Postgraduate Excellence 2017. He was the recipient of the 2020 Defence Science and Technology Eureka Prize for Outstanding Science in Safeguarding Australia.

Benjamin J. Eggleton (Fellow, IEEE) received the bachelor's (Hons.) degree in science and the Ph.D. degree in physics from The University of Sydney, Sydney, NSW, Australia, in 1992 and 1996, respectively. In 1996, he joined Bell Laboratories, Lucent Technologies, Murray Hill, NJ, USA, as a Postdoctoral Member of Staff, and then transferred to the Department of Optical Fiber Research. In 2000, he became the Research Director within the Specialty Fiber Business Division, Lucent Technologies. He is currently a Professor of physics with The University of Sydney, the Director of The University of Sydney Nano Institute (Sydney Nano), and the Co-Director of the NSW Smart Sensing Network (NSSN). He was the Director of the ARC Centre of Excellence for Ultrahigh Bandwidth Devices for Optical Systems (CUDOS). He is the author or co-author of more than 500 journal publications. His research interests include nonlinear optics, all-optical signal processing, optical communications, photonic crystals, and stimulated Brillouin scattering. He is a Fellow of the Australian Academy of Science, Australian Academy of Technology and Engineering (ATSE), and Optical Society of America. He was the recipient of the 2020 WH Beattie Steel Medal from the Australian and New Zealand Optical Society, Pawsey Medal from the Australian Academy of Science, 2004 Malcolm McIntosh Prize for Physical Scientist of the Year, 2003 International Commission on Optics Prize, 1998 Adolph Lomb Medal from the Optical Society of America, Distinguished Lecturer Award from the IEEE/Lasers and Electro-Optics Society, and Research and Development 100 Award. He was the President of the Australian Optical Society during 2008–2010. He is currently an Editor-in-Chief of *APL Photonics*.